



1 An Updated Parameterization of the Unstable Atmospheric Surface 2 Layer in WRF Modeling System

3 Prabhakar Namdev¹, Maithili Sharan¹, Piyush Srivastava², Saroj K. Mishra¹

4 ¹Centre for Atmospheric Sciences, Indian Institute of Technology Delhi, New Delhi, 110016, India

5 ²Centre of Excellence in Disaster Mitigation and Management, Indian Institute of Technology Roorkee, Roorkee, 247667,
6 India

7 *Correspondence to:* Prabhakar Namdev (Prabhakarnmsc587@gmail.com)

8 **Abstract.** Accurate parameterization of atmospheric surface layer processes is crucial for weather forecasts using numerical
9 weather prediction models. Here, an attempt has been made to improve the surface layer parameterization in the Weather
10 Research and Forecasting Model (WRFv4.2.2) by implementing similarity functions proposed by Kader and Yaglom (1990)
11 to make it consistent in producing the transfer coefficient for momentum observed over tropical region (Srivastava and Sharan
12 2015). The surface layer module in WRFv4.2.2 is modified in such a way that it contains all commonly used φ_m and φ_h under
13 convective conditions instead of the existing single functional form. The updated module has various alternatives of φ_m and
14 φ_h , which can be controlled by a flag introduced in the input file. The impacts of utilizing different functional forms have been
15 evaluated using the bulk flux algorithm as well as real-case simulations with the WRFv4.2.2 model. The model-simulated
16 variables have been evaluated with observational data from a flux tower at Ranchi (23.412N, 85.440E; India) and the ERA5-
17 Land reanalysis dataset. The transfer coefficient for momentum simulated using the implemented scheme is found to agree
18 well with its observed non-monotonic behaviour in convective conditions (Srivastava and Sharan 2022). The study suggests
19 that the updated surface layer scheme performs well in simulating the surface transfer coefficients and could be potentially
20 utilized for parameterization of surface fluxes in the numerical weather prediction model.

21 1 Introduction

22 Inadequate representation of near-surface turbulent processes adds significant uncertainty in both climate projections and
23 seasonal weather forecasts obtained from atmospheric models (Bourassa et al., 2013). Most of the numerical weather prediction
24 and general circulation models utilize Monin-Obukhov similarity theory (MOST; Monin and Obukhov 1954) to parameterize
25 surface turbulent fluxes. To estimate these fluxes and near-surface atmospheric variables, the theory utilizes similarity
26 functions of momentum (φ_m) and heat (φ_h) often prescribed as functions of ζ (stability parameter). However, the exact
27 functional forms for these functions have not been provided by MOST, rather it suggests some asymptotic predictions under
28 near neutral to very stable and unstable conditions which are tuned with field data. Over the years, researchers have developed
29 many functional forms for these functions based on the different experiments, conducted over different locations and have
30 separate expressions for stable and unstable stratifications (Webb, 1970; Businger, 1971; Carl et al., 1973; Dyer, 1974; Hicks,



31 1976; Holtslag and De Bruin, 1988; Brutsaert, 1992; Bruin, 1999; Wilson, 2001; Cheng & Brutsaert, 2005; Grachev et al.,
32 2007; Gryanik et al. 2020; Srivastava et al. 2020).

33 In most of the atmospheric models, the commonly used similarity functions under convective conditions are those
34 proposed by Businger (1966) and A. J. Dyer [1965, unpublished work; see Businger (1988)] and referred to as Businger-Dyer
35 (BD) functions. However, these functional forms are unable to follow the classical free convection limit. The study by Rao et
36 al. (1996) suggests that the MOST using Businger relations is unable to define transfer coefficient for momentum (C_D)
37 consistent with its observed behaviour, specifically at low wind convective conditions, indicating that MOST needs to be
38 modified in the (nearly) windless free convection limits. As a result, a revised scaling of heat flux for weakly forced convection
39 in the atmosphere has been proposed by Rao et al. (2006). Later, the issues of using BD functions in the surface layer scheme
40 based on the fifth-generation Pennsylvania State University-National Centre for Atmospheric Research Mesoscale Model
41 (MM5) of a regional scale model (Weather Research and Forecasting; WRF) have been reported in a study by Jimenez et al.
42 (2012). They implemented the new scheme (referred to as revised MM5 scheme; Jimenez et al., 2012) in WRF modeling
43 system and replaced the BD functions by those proposed by Fairall et al. (1996) (F96) under convective conditions. F96
44 functions are the combination of BD functions and the functions suggested by Carl et al. (1973) and are valid for the entire
45 range of atmospheric instability. Note that the most recent version of the WRF model still utilizes F96 functions under
46 convective conditions.

47 Srivastava and Sharan (2015) analyzed the observed behaviour of C_D over an Indian land surface and suggested that
48 the observed C_D shows non-monotonic behaviour with $-\zeta$, unlike the behaviour of predicted C_D from MOST based
49 parameterization using commonly used φ_m and φ_h (Businger et al., 1971; Carl et al., 1973; Fairall et al., 1996). Later, a
50 theoretical study by Srivastava and Sharan (2021) revealed that the three-sublayer model based on Kader and Yaglom (1990)
51 is able to predict C_D consistent with its observed non-monotonic behaviour. Note that the three-sublayer model has not yet
52 been incorporated and evaluated in WRF modeling framework. However, it is already being operational in the surface layer
53 scheme (Community Land Model; CLM) of National Centre for Atmospheric Research Community Atmosphere Model
54 version 5 (NCAR-CAM5) as well as Regional Climate Model (RegCM).

55 The study by Srivastava and Sharan (2021) also analyzed the possible uncertainties associated with the use of different
56 functional forms of φ_m and φ_h under convective conditions. To quantify the impacts of different functional forms, they
57 classified available φ_m and φ_h in four classes based on the exponents appearing in the expressions of φ_m and φ_h as (1)
58 functional forms having the exponents of φ_m and φ_h as $-1/4$ and $-1/2$, respectively (Businger et al. 1971; Hogstrom 1996).
59 (2) functional forms having the exponent of φ_m and φ_h as $-1/3$ (Carl et al. 1973). (3) functional forms having the exponent
60 of φ_m and φ_h as $-1/4$ and $-1/2$, respectively in near neutral conditions while $-1/3$ in very unstable conditions (Fairall et
61 al. 1996; Grachev et al. 2000; Fairall et al. 2003). (4) functional forms having the exponent of φ_m and φ_h as $-1/4$ and $-1/2$,
62 respectively in near neutral conditions however, $1/3$ for φ_m and $-1/3$ for φ_h in strong unstable conditions (Kader and
63 Yaglom 1990; Zeng et al. 1998). This study concluded that utilizing different functional forms of similarity functions in the
64 bulk flux algorithm results in a large deviation in the values of estimated fluxes. The detailed description of different functional



65 forms for φ_m and φ_h considered in different classes are given in Appendix B. We wish to highlight that the available
66 functional forms for φ_m and φ_h under convective conditions fall in one of the classes stated above.

67 The revised MM5 surface layer scheme of WRF model version 4.2.2 (WRFv4.2.2) employed φ_m and φ_h based on
68 Fairall et al. (1996), which, belong to class 3. As a result, this scheme is not appropriate in producing C_D consistent with its
69 observed behaviour, specifically over the Indian land as stated above. Recently Namdev et al. (2023) argue that the
70 performance of NWP models varies a lot over different seasons and surface types depending upon the functional behaviour of
71 φ_m and φ_h . Thus, to enhance the potential applicability of WRF modeling framework, this study attempted to incorporate all
72 the commonly used similarity functions under convective conditions along with KY90 as well as existing functional forms in
73 the revised MM5 surface layer scheme of WRFv4.2.2. A namelist flag has been introduced in WRF model to choose between
74 various φ_m and φ_h in the modified scheme. The modified surface layer scheme proposed in this study has been evaluated
75 using offline simulations with bulk flux algorithm as well as the real-case simulations with WRFv4.2.2 during the pre-monsoon
76 season (March-April-May) of 2009 over a domain centered around the location of the flux tower installed at Ranchi (23.412N,
77 85.440E), India.

78 2 Methodology and data

79 2.1 Surface flux computation in the WRF modeling system

80 The Monin-Obukhov similarity theory serves as the foundation for the surface layer parameterization (revised MM5 scheme)
81 in the WRF model, and the surface turbulent fluxes are calculated based on the bulk approach using bulk transfer coefficients
82 for momentum (C_D) and heat (C_H) (Namdev et al., 2024; Srivastava et al., 2021; Srivastava and Sharan, 2021). A brief
83 description and different numerical expressions used in the computation of surface fluxes in WRF model are provided in
84 Appendix A.

85 The default version of the revised MM5 scheme in WRF model utilizes similarity functions suggested by Cheng and
86 Brutsaert (2005) under stable atmospheric conditions ($\zeta > 0$), which are developed using CASES-99 dataset. The integrated
87 forms of functions proposed by Cheng and Brutsaert are

$$88 \psi_m(\zeta) = -a \ln(\zeta + [1 + \zeta^b]^{1/b}), \quad \zeta > 0 \quad (1)$$

$$89 \psi_h(\zeta) = -c \ln(\zeta + [1 + \zeta^d]^{1/d}), \quad \zeta > 0 \quad (2)$$

90 where $d = 1.1, c = 5.3, b = 2.5$ and $d = 6.1$.

91 On the other hand, the similarity functions for unstable atmospheric surface layer ($\zeta < 0$) are those proposed by
92 Fairall et al. (1996). The corresponding integrated functional forms ψ_m and ψ_h are defined as:

$$93 \psi_\alpha(\zeta) = \frac{\Psi_{\alpha_{BD}}(\zeta) + \zeta^2 \Psi_{\alpha_{conv}}(\zeta)}{1 + \zeta^2}, \quad \alpha = m, h. \quad (3)$$



94 where $\psi_{\alpha_{BD}}$ and $\psi_{\alpha_{conv}}$ denote the integrated functional forms based on Businger and Dyer, and Carl et al. (1973),
95 respectively. The expressions for $\psi_{\alpha_{BD}}$ and $\psi_{\alpha_{conv}}$ are

$$96 \quad \psi_{m_{BD}}(\zeta) = 2 \ln\left(\frac{1+x}{2}\right) + \ln\left(\frac{1+x^2}{2}\right) - 2 \tan^{-1} x + \frac{\pi}{2}, \quad (4)$$

$$97 \quad \psi_{h_{BD}}(\zeta) = 2 \ln\left(\frac{1+x^2}{2}\right), \quad (5)$$

98 in which $x = (1 - 16\zeta)^{1/4}$ and

$$99 \quad \psi_{\alpha_{conv}} = \frac{3}{2} \ln(y^2 + y + 1/3) - \sqrt{3} \tan^{-1}(2y + 1/\sqrt{3}) + \frac{\pi}{\sqrt{3}} \quad (6)$$

100 with $y = [1 - \beta_{m,h}\zeta]^{1/3}$. The values of the constants β_m and β_h are taken as 10 and 34 based on Grachev et al. (2000).

101 2.2 Implementation of different similarity functions

102 In this section, we briefly describe the implementation of different similarity functions under unstable stratification of surface
103 layer parameterization of WRFv4.2.2.

104 2.2.1 Functions by Businger et al. (1971) (BD71)

105 Similarity functions suggested by Businger et al. (1971) are based on the KANSAS dataset. These functions do not satisfy the
106 classical free convection limit as predicted by the MOST. These functions are already implemented in the old version of the
107 MM5 surface layer scheme (Grell et al., 1994) in WRF model. The integrated functional forms (ψ_m and ψ_h) for φ_m and φ_h
108 stated in Appendix B (Eqs. B1 and B2) are given in Eqs. (4) and (5). BD71 functions have already been used in the old
109 version of the MM5 scheme.

110 2.2.2 Functions by Carl et al. (1973) (CL73)

111 Carl et al. (1973) proposed an expression of similarity functions φ_m and φ_h valid for the stability range $-10 \leq \zeta \leq 0$. The
112 expressions for φ_m and φ_h are given in Eqs. (B3, and B4: Appendix B). The similarity functions proposed by Carl et al.



113 (1973) have not been analyzed in the surface layer scheme of WRF model. The integrated forms (ψ_m and ψ_h) of similarity
 114 functions φ_m and φ_h are given in Eqn. (6).

115 2.2.3 Functions by Kader and Yaglom (1990) (KY90)

116 Kader and Yaglom (1990) introduced a three-sublayer model for convective conditions. The three sublayers are categorized
 117 based on ζ values as (1) the dynamic sublayer which corresponds to near neutral conditions, (2) the dynamic convective
 118 sublayer which corresponds to moderately unstable conditions and (3) the free convective conditions. The present study
 119 utilized φ_m and φ_h expressions (given in Eqns. B9, and B10 in Appendix B) that are being used in the surface layer scheme
 120 (CLM4.0; Zeng et al. 1998) of NCAR-CAM5 model. The corresponding integrated forms for φ_m and φ_h are

$$121 \quad \psi_m(\zeta) = \begin{cases} \psi_{m1}(\zeta_m) + \ln \frac{\zeta}{\zeta_m} - 1.14[(-\zeta)^{1/3} -], & \zeta \leq -1.574 (= \zeta_m) \\ \psi_{m1}(\zeta) = 2 \ln \left(\frac{1+x}{2} \right) + \ln \left(\frac{1+x^2}{2} \right) - 2 \tan^{-1} x + \frac{\pi}{2}, & -1.574 < \zeta < 0 \end{cases} \quad (7)$$

$$122 \quad \psi_h(\zeta) = \begin{cases} \psi_{h1}(\zeta_h) + \ln \frac{\zeta}{\zeta_h} - 0.8[(-\zeta)^{-1/3} - (-\zeta_h)^{-}], & \zeta \leq -0.465 (= \zeta_h) \\ \psi_{h1}(\zeta) = 2 \ln \left(\frac{1+x^2}{2} \right), & -0.465 < \zeta < 0 \end{cases} \quad (8)$$

123 where $x = (1 - 16\zeta)^{1/4}$.

124 Note that all the functions stated above have been incorporated in the revised MM5 surface layer scheme of
 125 WRFv4.2.2 and can be used in place of F96 functions already employed in the model. Here, we have introduced a new surface
 126 layer module where different options for φ_m and φ_h can be controlled using an appropriate value of namelist parameter
 127 (psimhu_opt). The parameter psimhu_opt is added under the physics section of the namelist file. The variable psimhu_opt can
 128 have values 0, 1, 2, and 3 for different options for functions F96 (default), BD71, CL73, and KY90 respectively. A brief
 129 structure and different choices for psimhu_opt based on different incorporated and default functional forms of φ_m and φ_h in
 130 the default and modified revised MM5 scheme are shown in Figure 1.

131 2.3 Characteristics of default and incorporated similarity functions

132 The expressions of φ_m and φ_h for different functional forms utilized in this study are stated in Appendix B. Figure S1
 133 (supplementary material) shows the variation of different (a) φ_m and (b) φ_h under moderately to strongly unstable conditions.
 134 It is evident from Figure S1 that all the different functional forms provide similar values of φ_m and φ_h in near neutral to
 135 moderately unstable conditions (up to $\zeta = -0.1$ approximately). However, at higher instabilities one can expect noticeable
 136 differences between different functional forms of φ_m and φ_h . Note that the functional forms for φ_m corresponding to BD71



137 and CL73 decrease continuously on increasing instability; however, φ_m corresponding to KY90 functional forms show
138 decreasing behaviour in near-neutral to moderately unstable conditions and attain a minimum at $\zeta = -1.574$, and, as the
139 instability further increases, it starts increasing with $-\zeta$ (Figure S1a). This implies that φ_m based on class 4 functions shows
140 non-monotonic behaviour which contradicts the classical MOST prediction. On the other hand, in case of φ_h , all the functional
141 forms provide continuously decreasing behaviour of φ_h from near neutral to moderately unstable conditions (Figure S1b).

142 Figure 2 illustrates the variation of default (F96) and different incorporated integrated similarity functions ψ_m and
143 ψ_h (BD71, CL73, and KY90) with respect to $-\zeta$. It is observed from Figure 2a that ψ_m corresponding to F96, BD71, and
144 CL73 functional forms increases continuously with $-\zeta$ in moderately to strong unstable conditions. However, a non-
145 monotonic behaviour has been observed for ψ_m corresponding to KY90 functions implying it first increases with $-\zeta$ and
146 reaches a maximum at $\zeta = -1.574$ and then starts decreasing as instability further grows. On the other hand, ψ_h corresponding
147 to all the considered functional forms increases continuously in near neutral to strong unstable conditions. However, the rate
148 of increase is slightly higher for F96 in comparison to other three functions while ψ_h is found to be almost comparable obtained
149 from other three functions BD71, CL73, and KY90 (Fig. 2b).

150 2.4 Observational data for model evaluation

151 For the evaluation of the real-case simulations, observational data derived from the micrometeorological tower installed at
152 Ranchi (India) has been utilized (Srivastava and Sharan, 2019; Srivastava et al., 2020; 2021). The dataset (Ranchi data) is
153 derived from an instrument mounted on a 32-m tall tower at the Birla Institute of Technology Mesra in Ranchi, India (Dwivedi
154 et al., 2014). A fast response sensor (CSAT3 Sonic Anemometer) at a height of 10 m with an average elevation 609 m above
155 sea level provides the temperature and the three components of wind at a 10 Hz frequency. The eddy covariance technique
156 (Stull 1988) is used to estimate heat and momentum fluxes at one-hour time resolution, however the hourly temperature at 2
157 m is determined by averaging temperature observations available at a temporal scale of 1 minute from the slow response
158 sensors located at logarithmic heights on the same tower. Sharan and Srivastava (2016); Srivastava and Sharan (2015;
159 2019) provided comprehensive descriptions of the dataset, quality control process and site. Apart from this we have also
160 utilized the ERA5-Land reanalysis dataset available at $0.10^\circ \times 0.10^\circ$ spatial resolution to evaluate the spatial distribution of
161 the model simulated near surface atmospheric variables. For consistency, we have regridded the model output to the same grid
162 resolution of reanalysis/observed dataset.

163 3 Numerical simulations

164 Impacts of incorporated similarity functions together with the existing functional forms in surface layer scheme of WRFv4.2.2.
165 For evaluation purpose, offline experiments as well as real case simulations have been conducted. The offline simulations are
166 conducted using the transcendental relation given in Eqn. (A7 in Appendix A) to test the performance of incorporated functions
167 without feedback to the atmosphere. In offline simulations, the value of ζ is estimated by calculating the root of least magnitude



168 of Eqn. (A7 in Appendix A) for a given value of Ri_B . Once ζ is calculated then utilizing it in Eqns. (A8) and (A9), the values
169 of C_D and C_H can be estimated. For the computation, z is taken as 10 m and Ri_B is in the range $-2 \leq Ri_B \leq 0$. The offline
170 simulations are carried out over three different surface types by considering surface roughness (z_0) to be 0.01 m (smooth
171 surface), 0.1 m (transition surface) and 1 m (rough surface) to analyze the impact of roughness of underlying surface on the
172 simulation of ζ , C_D and C_H .

173 On the other hand, the real-case simulations with incorporated similarity functions have been done using WRFv4.2.2
174 model over an Indian land site during the pre-monsoon (March-April-May; MAM) season of the year 2009. The simulations
175 have been conducted over a nested domain centred around the location of a micrometeorological tower installed at Ranchi
176 (23.412°N , 85.44°E), India (Figure 3). Domain d01 (6×6 km) consists of 233 east-west and 210 north-south grid points and
177 domain d02 (2×2 km) consists of 223 east-west and 196 north-south grid points which covers 1398×1260 km² and
178 446×392 km² spatial area around the centre point, respectively. Each domain was configured with 50 vertical eta levels
179 from surface to top of the atmosphere. We kept five vertical levels below 100 m height. Initial and boundary conditions were
180 taken from ERA5 global atmospheric reanalysis dataset at a resolution of $0.25^\circ \times 0.25^\circ$ and boundary conditions were forced
181 every 6 hours. For land use and land cover (LU/LC) information, we have used dataset from MODIS (Moderate Resolution
182 Imaging Spectroradiometer; Friedl et al., 2002). Various physical parameterizations utilized in the simulations are listed in
183 Appendix C. In this study, four sets of simulations were carried out, as given in Table 1.

184 The whole simulation period is divided into segments of 4 days with 24 h overlapping time between different
185 segments to ensure continuity. The model is initialized at 0000 UTC of 1st day of each simulation and runs for 96 hours. In
186 order to avoid the potential spin-up problems at the beginning of the simulation, we discard the first day of each simulation as
187 spin up time and consider the last three days for the analysis (Jimenez et al., 2010; 2012).

188 For the evaluation of the real-case simulations, different statistical parameters such as mean absolute error (MAE),
189 root mean square error (RMSE), mean bias (MB), index of agreement (IOA), different measures of correlation coefficient
190 (CC), mean bias (%) (bias), and standard deviation of the model predicted output normalized by that of the observations are
191 used. Brief description of the performance indicators for validation utilized in the present study is stated in Appendix C.

192 4 Results

193 4.1 Offline simulations

194 The offline simulations (Exp1, Exp2, and Exp3) have been conducted utilizing incorporated functions (BD71, CL73, and
195 KY90) together with CTRL simulation using F96 functions for three different roughness lengths for momentum (z_0), which
196 are representative of smooth ($z_0 = 0.01$ m), transition ($z_0 = 0.1$ m), and rough ($z_0 = 1.0$ m) surfaces. The simulated results
197 for ζ (a_1 , a_2 , and a_3) with Ri_B , C_D (b_1 , b_2 , and b_3) and C_H (c_1 , c_2 , and c_3) with ζ across various surface types and sublayers



198 have been analyzed (Figure 4). The different sublayers associated with convective stratification include dynamic (DNS),
199 dynamic-dynamic convective transition (DNS-DCS), dynamic convective (DCS), dynamic convective-free convective
200 transition (DCS-FCS), and free convective (FCS) (Srivastava and Sharan, 2021). It is observed that the simulated values of ζ
201 for smaller values of Ri_B (i.e., in DNS to DCS) from different experiments are found to be identical to the CTRL simulation
202 (Figure 4a1-3). However, in FCS, large deviations have been observed in the simulated values of ζ for a given Ri_B from
203 different experiments (Figure 4a1-3). Notably, Exp1, Exp2, and CTRL simulations predict relatively smaller absolute values
204 of ζ for a given value of Ri_B . However, Exp3 is found to produce a relatively larger magnitude of ζ for a given value of Ri_B .
205 This behaviour is observed to be consistent for all the values of ratio z/z_0 (Figures 4a1-3) representative of smooth,
206 transitional, and rough surfaces. The substantially larger magnitude of ζ for a given value of Ri_B and the smaller values of ψ_m
207 and ψ_h (Figure 2) in Exp3 implies that the momentum and heat fluxes predicted in Exp3 will be smaller than those anticipated
208 in Exp1, Exp2, and CTRL simulation.

209 Figure 4b1-3 shows the variation of C_D with ζ predicted in CTRL simulation and Exp1-3 over different surfaces.
210 Notice that the C_D values predicted in Exp1, Exp2, and CTRL simulations are substantially higher and continue to rise as
211 instability progresses from DCS to FCS. On the other hand, Exp3 simulates significantly smaller values of C_D as compared to
212 the other three experiments. It is important to highlight that C_D from Exp3 (KY90 functions) shows a non-monotonic
213 behaviour, which is consistent with the observed behaviour of C_D over the Indian region reported in the literature (Srivastava
214 and Sharan, 2019; 2021). Note that this non-monotonic behaviour is consistent for all three cases of different roughness lengths
215 (Figure 4b1-3).

216 On the other hand, across all three surfaces, it is observed that the values of C_H predicted in all four experiments
217 increases with increasing instability (Figure 4c1-3). While the rate of increase of C_H in Exp3 is noticeably slower. Moreover,
218 Exp1, Exp2, and CTRL simulation predict almost similar values over all three types of surfaces. Noticeably, C_H also exhibits
219 non-monotonic behaviour with ζ over rough surfaces, which contradicts the predictions of the other three experiments. In
220 addition, it is important to note that C_D and C_H predicted by Exp3 are found to bound by twice their near-neutral values, while
221 the other experiments predict continuously increasing values of C_D and C_H on increasing instability.

222 Hence, it is evident from the offline experiments that the functional forms adopted in Exp1 (BD71), Exp2 (CL73),
223 and CTRL (F96) predict values of ζ , C_D , and C_H that are almost same. However, using KY90 functions compared to other
224 commonly used φ_m and φ_h , one can expect a significant reduction in the estimated values of transfer coefficients in
225 moderately to strongly unstable stratification.

226 4.2 Real-case simulations

227 In this section, observational and reanalysis datasets have been used to analyze the simulations performed with WRFv4.2.2
228 utilizing different incorporated and default φ_m and φ_h . The model simulated output has been extracted at the location of flux
229 tower and compared against the observations derived from the flux tower installed at Ranchi (23.412N, 85.440E), India. The



230 mean spatial patterns of certain variables averaged over daytime (04:00-12:00 UTC) have been compared against the ERA5-
231 Land reanalysis dataset. Further, to access the effects of incorporated functions under free convective conditions, the mean
232 spatial patterns of considered variables averaged across strong convective conditions (hours in which $\zeta < -10$ over most of
233 the domain) have been analyzed against respective hours of ERA5-Land reanalysis data. Bilinear interpolation has been used
234 to interpolate the model output to the same grid resolution as the ERA5-Land data in order to allow a consistent comparison.

235 **4.2.1 Evaluation against observations derived from flux tower installed at Ranchi (India)**

236 Figure 5 depicts the variation of (a) ζ with Ri_B , (b) C_D , and (c) C_H with ζ from different experiments (Exp1, Exp2, and Exp3)
237 and CTRL simulation. The variation of simulated ζ with Ri_B , C_D , and C_H with ζ is found to be consistent with offline results.
238 The values of simulated variables are found to be identical in DNS to DCS sublayers for all the experiments; however, in FCS,
239 substantial differences between different experiments (Figures. 5a, b, and c) have been observed. Simulated ζ for a given Ri_B
240 in Exp2 and CTRL simulation are similar and found to be smaller in magnitude than Exp1 and Exp3 in FCS. However, the
241 absolute values of ζ in Exp3 (KY90 functions) are significantly larger in FCS than in all other experiments.

242 Figure 5b shows the variation of simulated C_D with ζ from different experiments. Yellow crosses denote the variation
243 of observed C_D with ζ at the location of flux tower (Figure 5b). It is observed that the observed C_D increases as the instability
244 increases from DNS to DCS and has the maximum value in the DCS (at $\zeta = -0.1$ approx.) and then starts to decrease as
245 instability grows further from DCS to FCS. It is evident that C_D simulated using φ_m and φ_h based on class 4 functions (Exp3)
246 exhibits non-monotonic behaviour (Figure 5b), which is consistent with the observed behaviour of C_D (Srivastava and Sharan,
247 2015; 2021). On the other hand, C_D simulated using φ_m and φ_h based on the first three classes (Exp1, Exp2, and CTRL
248 simulation) increases continuously as instability grows from DNS to FCS (Figure 5b). However, it is found that the C_D
249 predicted from the original forms of class 4 functions (EXP3) does not perfectly match with its observed behaviour, as the
250 predicted C_D starts decreasing at ζ lying in FCS, which is different from that observed, i.e., ζ lying in DCS. In view of it,
251 Srivastava and Sharan (2021) tuned the original forms of class 4 functions by enforcing the matching of the point at which
252 both observed and model predicted C_D attain their maximum value. However, more studies in terms of predicting the observed
253 variation of the non-dimensional vertical gradients of mean wind speed and temperature with ζ are essential to further tune the
254 original KY90 functions for the Indian region using observed data from various locations under different seasons.

255 The magnitude of C_D predicted in Exp3 is significantly smaller than that simulated from other experiments as well as
256 CTRL simulation, specifically in FCS. This may be due to the large differences between the KY90 functional forms of ψ_m
257 and ψ_h and other forms of functions. We wish to highlight that utilizing KY90 (Exp3) functions in the revised MM5 scheme
258 of WRF model makes it consistent in predicting C_D with its observed behaviour over the Indian region. The variation of
259 simulated C_H with ζ from different experiments is shown in Figure 5c. C_H simulated from Exp1-3 as well as CTRL simulation
260 shows continuously increasing behaviour with ζ . The magnitude of simulated C_H from CTRL simulation and Exp1-2 is



261 relatively higher than that of Exp3 in FCS beyond $\zeta < -10$ (approximately). It is also evident that at higher instabilities, even
262 C_H shows non-monotonic behaviour with ζ (Figure 5c).

263 The analysis presented here indicates that the KY90 functions in the revised MM5 surface layer scheme are found to
264 be appropriate in producing non-monotonic behaviour of C_D consistent with its observed nature. However, all other functional
265 forms of φ_m and φ_h produce C_D , which increases continuously with ζ from DNS to FCS.

266 To quantify the uncertainties involved in the simulated surface fluxes and certain near-surface variables using KY90
267 (Exp3) as well as other functional forms (Exp1-2 and CTRL simulation), model simulations have been compared against the
268 observations. Figure 6 compares the model-simulated (a) u_*^2 ($\text{m}^2 \text{s}^{-2}$) (representative of momentum flux), (b) SHF (W m^{-2})
269 (sensible heat flux), (c) U_{10} (m s^{-1}) (10-m wind speed), and (d) T_{2m} (K) (2-m temperature) with the observed data obtained
270 from the flux tower at Ranchi (23.412N, 85.440E), India. The model output was extracted at a single grid point closest to the
271 flux tower to allow a consistent comparison. In Figure 7, a Taylor diagram is displayed along with the normalized standard
272 deviations and correlations of considered variables. Figure 8 shows the scatter plot between CC vs. RMSE for considered
273 variables simulated using different experiments. In case of u_*^2 , Exp1 and Exp2 are found to be comparable to the CTRL
274 simulation, while Exp3 considerably improved the simulation of u_*^2 (Figures 6a, 7 and 8). Exp3 reduced MAE (RMSE) from
275 0.088 (0.156) $\text{m}^2 \text{s}^{-2}$ to 0.082 (0.144) $\text{m}^2 \text{s}^{-2}$ (Table 2; Figures 7 and 8) and improved the CC (0.742) and IOA (0.843) for u_*^2
276 (Table 2). A Q-Q plot is shown in Figure S2a (supplementary material) suggesting that Exp3 (KY90 functions) is found to be
277 slightly better than all other experiments and CTRL simulation for u_*^2 . For SHF, all the experiments are comparable to the
278 CTRL simulation; however, Exp3 shows less scatter than other experiments (Figure 6a).

279 In case of U_{10} , Exp3 shows less scatter and appears to be closer to the observations than other experiments (Figure
280 6c). Exp3 noticeably improved the simulation of U_{10} by reducing MAE (RMSE) from 1.198 (1.543) m s^{-2} to 1.164 (1.466) m
281 s^{-2} and MB up to 5 % (Figures 6c, and 7; Table 2). It considerably improved the CC (IOA) for U_{10} from 0.659 (0.729) to 0.681
282 (0.751) (Figure 7 and Table 2). A Q-Q plot (Figure S2b: supplementary material) reveals that Exp3 is observed to be better
283 than all other experiments and CTRL simulation for U_{10} . Thus, the KY90 functions in the surface layer scheme of the WRF
284 model considerably improve the model in simulating U_{10} (Figures. 6c, 7, 8, and S2b) at the location of the flux tower. Further,
285 in case of T_{2m} , Figures 7 and 8 exhibit that all the experiments are found to be comparable with the CTRL simulation.

286 4.2.2 Evaluation of mean spatial distribution of simulated variables against ERA5-Land reanalysis data during daytime

287 In this section, mean spatial distribution of simulated variables from different experiments as well as CTRL simulation
288 averaged during daytime (04:00-12:00 UTC) for entire simulation period, is compared with the ERA5-Land reanalysis data.
289 Figure 9 depicts the mean spatial patterns of simulated ζ ($= \frac{z}{L}$) (a1–4), C_D (c1-c4), and C_H (e1-4) from CTRL simulation
290 and other experiments, as well as their differences with respect to CTRL simulation. It is observed that the absolute value of ζ
291 simulated in Exp3 (KY90 functions) is much lower than CTRL simulation (Figure 9b3) across the whole domain, which is



292 consistent with Figure 5a and offline simulations presented in Figure 4(a1-3). This could be because the magnitude of KY90
293 functions (φ_m and φ_h) are smaller than the functions employed in default scheme (CTRL simulation).

294 On the other hand, Exp1 also provides slightly smaller absolute values of ζ (Figure 9b1), while Exp2 is almost
295 comparable to the CTRL simulation (Figure 9b2). Model simulated C_D is found to be smaller in Exp3 than CTRL simulation
296 (Figure 9d3), while Exp1 and Exp2 provide comparable values of C_D to CTRL simulation (Figure 9d1-2). In the case of C_H ,
297 the simulated values from different experiments are observed to be comparable to the CTRL simulation over whole study
298 domain (Figure 9f1-3). These large differences between C_D simulated from different experiments may be related to the fact
299 that only φ_m functions are involved in the computation of C_D (Eqn. A8 in Appendix A), and the differences between φ_m are
300 comparatively more than φ_h , so are the differences in C_D . The hatched regions in Figure 9 shows the differences between
301 simulated variables from different experiments with respect to CTRL simulation are statistically significant at 95% confidence
302 level.

303 The differences in C_D reflected further in the simulated u_*^2 $m^2 s^{-2}$ (a measure of momentum flux) in Exp3 (Figure
304 10b3). Exp3 significantly reduced the simulated values compared to the CTRL simulation over some parts of the domain
305 (Figure 10b3), while in Exp1 and Exp2 values are comparable with the CTRL simulation (Figure 10b1-2). In case of SHF and
306 LHF, the mean spatial distribution from all the experiments is found to be consistent with the ERA5-Land reanalysis data, and
307 the magnitude of differences between model simulation and ERA5-Land data is comparable for all the experiments (Table S1;
308 supplementary material).

309 For T_{2m} (upper panel of Figure 11), T_s (middle panel of Figure 11), and U_{10} (lower panel of Figure 11), mean spatial
310 distribution from different experiments and CTRL simulation agreed well with slightly varying magnitude to the ERA5-Land
311 reanalysis data. A warm bias up to 2 K (3 K) was observed for T_{2m} (T_s) simulated from different experiments and CTRL
312 simulation over most of the domain. For T_{2m} , bias, RMSE, and PCC between different experiments together with CTRL
313 simulation and ERA5-Land reanalysis data are found to be comparable (Table S1; supplementary material). However, Exp3
314 slightly improved the PCC from 0.503 to 0.512 for T_s (Table S1; supplementary material). Further, in the case of U_{10} , all the
315 simulations exhibit overprediction over the whole domain (lower panel of Figure 11: b1-4) and Exp3 is observed to be slightly
316 better than all other experiments as well as CTRL simulation as it reduced bias% (RMSE) from 32.283 (0.544) $m s^{-2}$ to 32.057
317 (0.539) $m s^{-2}$ and improved the PCC from 0.899 to 0.911 (Table S1: supplementary material).

318 **4.2.3 Evaluation of incorporated functions during strong unstable conditions with respect to ERA5-Land reanalysis** 319 **data**

320 This section describes the impacts of utilizing different similarity functions (φ_m and φ_h) on simulated variables during highly
321 convective regime (i.e., $\zeta < -10$) with respect to the ERA5-Land reanalysis dataset. Since the functional forms of ψ_m and ψ_h
322 are identical in near neutral to moderately unstable conditions, however, in strong unstable conditions, the differences between
323 different functional forms are more pronounced. Thus, the corresponding differences in the simulated values of considered



324 variables are expected to be more pronounced during highly convective regimes. For this purpose, the model output has been
325 extracted for those hours in daytime which show ζ smaller than -10 over most of the domain and compared with the respective
326 hours of ERA5-Land reanalysis data.

327 Figure S3 (Supplementary material) depicts the mean spatial distribution of ζ (a1-4), C_D (c1-4), and C_H (e1-4) as well
328 as their deviations from CTRL simulation. Notice that the magnitude of differences for all variables (ζ , C_D , and C_H) in this
329 case are found to be larger than the case of mean spatial patterns averaged during the whole daytime (section 6.2.2). It is
330 evident from Figure S3b3 (supplementary material) that Exp3 produce large absolute values of ζ and smaller values of C_D and
331 C_H (Figures S3b3, d3 and f3: supplementary material) than all other experiments and the CTRL simulation. While Exp1 and
332 Exp2 are found to be comparable to the CTRL simulation for both C_D and C_H (Figures S3d1-2 and f1-2).

333 The model simulations for T_{2m} and T_s do not capture the spatial patterns well in comparison to ERA5-Land data
334 (Figures S4a1-5 and S5a1-5: supplementary material). All experiments, as well as the CTRL simulation, exhibit overprediction
335 across the whole domain (Figures S4b1-4 and S5b1-4). We wish to highlight that the differences between various experiments
336 and CTRL simulation are seen up to 0.5 K for T_{2m} (Figure S4c1-3) as well as T_s (Figure S5c1-3) which is slightly higher than
337 the case of mean spatial patterns averaged over whole daytime (upper and middle panels of Figure 11). For T_{2m} , it is evident
338 from Figure S4 (supplementary material) and Table 3 that Exp3 noticeably reduced the bias% (RMSE) from 0.635 (2.133) K
339 to 0.623 (2.102) K and improved the PCC from 0.435 to 0.461 (approximately 6%). In case of T_s as well, Exp3 slightly
340 improved the PCC and reduced the bias% (RMSE) from 1.259 (4.013) K to 1.243 (3.972) K (Table 3 and Figure 12).

341 For U_{10} , the mean spatial patterns simulated using different experiments agreed well with the ERA5-Land reanalysis
342 data (Figure S6a1-5: supplementary material) and the magnitude of biases is found to be up to 1 m s^{-1} . Exp3 outperformed all
343 other experiments and the CTRL simulation by lowering the bias% from -4.962 to -0.284 m s^{-1} and improved the PCC from
344 0.343 to 0.364 with comparable RMSE values (Figures S6 and 12; Table 3).

345 **5 Summary and concluding remarks**

346 In the present study, the revised MM5 surface layer scheme of the WRFv4.2.2 model has been modified to incorporate φ_m
347 and φ_h suggested by Kader and Yaglom (1990) to make it consistent in producing the transfer coefficient for momentum (C_D)
348 in line with its observed behaviour. The revised MM5 scheme is modified in such a way that it contains all commonly used
349 φ_m and φ_h under convective conditions instead of a single functional form. Various alternatives of φ_m and φ_h in the modified
350 scheme can be controlled by a flag (psimhu_opt) that has been introduced in the physics section of the namelist file. The
351 impacts of utilizing different functional forms of φ_m and φ_h in the proposed scheme have been evaluated using offline
352 simulations (with bulk flux algorithm) as well as real-case simulations with WRFv4.2.2 model. The model-simulated surface
353 turbulent fluxes and certain near-surface variables have been compared with observational data from a flux tower at Ranchi
354 (23.412N, 85.440E; India), and the spatial patterns have been evaluated with the ERA5-Land reanalysis dataset.



355 Offline simulations indicate that at nearly neutral to moderately unstable conditions, ζ simulated using various
356 functional forms of φ_m and φ_h is comparable, and as the instability grows (free convective conditions), the differences
357 between different experiments become more pronounced. This might be connected to the corresponding variations between
358 different functional forms of similarity functions in the respective regimes. Similarly, for simulated C_D , Exp3 (KY90 functions)
359 demonstrates nonmonotonic behaviour with $-\zeta$ across all three surface types (representing smooth, transition, and rough
360 surfaces), which is consistent with its observed behaviour. However, all other experiments and CTRL simulation indicate
361 continuously increasing C_D with $-\zeta$ from near neutral to free convective conditions over all three surface types, which is
362 inconsistent with its observed behaviour over the study domain. The non-monotonic behaviour of C_D in Exp3 (KY90 functions)
363 may be associated to the analogous non-monotonic behaviour of the corresponding ψ_m in the respective regime.

364 In real-case simulations, the model simulated ζ , C_D and C_H are found to be consistent with the offline simulations.
365 The variation of C_D in Exp3 (KY90 functions) with $-\zeta$ is observed to be nonmonotonic, as reported in offline simulations and
366 found to be consistent with its observed behaviour. This indicates that the KY90 functions in the surface layer scheme of the
367 WRF model make it compatible in producing C_D consistent with its observed behaviour over Indian land. As compared with
368 the observations over Ranchi (India), the simulations using KY90 (Exp3) functions are found to perform better for most of the
369 considered variables compared to all other experiments. Further, in the mean spatial distribution averaged during daytime
370 (04:00–12:00 UTC) over the entire simulation period, the significant increase in absolute value of ζ from Exp3 resulted in a
371 noticeable reduction in the values of C_D and C_H , which further impacted the simulated values of T_s , T_{2m} , and U_{10} . When
372 compared with the ERA5-Land reanalysis data, the spatial patterns for T_{2m} , T_s , and U_{10} from Exp3 (KY90 functions) provided
373 more consistent results. A reduction has been observed in bias (%) and RMSE values for T_s , and U_{10} . Moreover, in case of
374 highly convective regime ($\zeta < -10$), Exp3 (KY90 functions) slightly improved the performance of the model by reducing the
375 bias (%) and RMSE for T_{2m} , T_s , and U_{10} and increasing the correlation to some extent.

376 Thus, it is concluded that the similarity functions proposed by Kader and Yaglom (1990) (KY90 functions; Exp3) are
377 found to be more appropriate for use in the WRF model as they can simulate C_D consistent with its observed behaviour and
378 improve the simulation for most of the considered variables over the study domain. However, due to the limited spatial
379 coverage of the domain considered in this study and the limited availability of observational data, KY90 functional forms need
380 to be further evaluated in the WRF modeling framework utilizing observations from other sites. The modified surface layer
381 scheme proposed in this study could enhance the potential applicability of the WRF modeling framework for the community
382 in investigating the role of different functional forms of similarity functions under convective conditions for selected
383 events/case studies such as extreme weather events, heat waves during summer, cyclonic storms, and fog predictions using the
384 WRF model.



385 Appendix A

386 This section consists of a brief description of the computation of surface turbulent fluxes in the revised MM5 surface layer
 387 scheme. In a homogeneous surface layer, the dimensionless wind and temperature gradients are defined as

$$388 \frac{kz}{u_*} \frac{\partial U}{\partial z} = \varphi_m(\zeta), \quad (\text{A1})$$

$$389 \frac{kz}{\theta_*} \frac{\partial \theta}{\partial z} = \varphi_h(\zeta). \quad (\text{A2})$$

390 where L denotes the Obukhov length scale and U is the wind speed at height z ; k represents the von Karman constant and its
 391 value is taken as 0.4. Integrating Eqns. (A1) and (A2) with respect to z leads to

$$392 U = \frac{u_*}{k} \left[\ln \left(\frac{z}{z_0} \right) - \left\{ \psi_m(\zeta) - \psi_m \left(\frac{z_0}{L} \right) \right\} \right], \quad (\text{A3})$$

$$393 (\theta_a - \theta_g) = \frac{\theta_*}{k} \left[\ln \left(\frac{z}{z_h} \right) - \left\{ \psi_h(\zeta) - \psi_h \left(\frac{z_h}{L} \right) \right\} \right] \quad (\text{A4})$$

394 in which ψ_m and ψ_h denote the integrated form of similarity functions φ_m and φ_h . The roughness lengths for momentum and
 395 heat are denoted by z_0 and z_h , respectively. ψ_m and ψ_h can be calculated from the following expression (e.g., Panofsky,
 396 1963):

$$397 \psi_m(\zeta) = \psi_h(\zeta) = \int_0^\zeta \frac{1 - \varphi_{m,h,q}(\zeta')}{\zeta'} d\zeta' \quad (\text{A5})$$

398 The bulk Richardson number (Ri_B) is given by:

$$399 Ri_B = \frac{g(\theta_a - \theta_g)(z - z_0)^2}{\theta U^2(z - z_h)} \quad (\text{A6})$$

400 Substituting the values of U and $(\theta_a - \theta_g)$ from Eqns. (A3) and (A4) in Eqn. (A6), one gets

$$401 Ri_B = \zeta \frac{\left[\left(1 - \frac{z_0}{z} \right)^2 \right] \left[\ln \left(\frac{z}{z_h} \right) - \left\{ \psi_h(\zeta) - \psi_h \left(\zeta \frac{z_h}{z} \right) \right\} \right]}{\left[\left(1 - \frac{z_h}{z} \right) \right] \left[\ln \left(\frac{z}{z_0} \right) - \left\{ \psi_m(\zeta) - \psi_m \left(\zeta \frac{z_0}{z} \right) \right\} \right]^2} \quad (\text{A7})$$

402 Note that Eqn. (A7) is a transcendental equation, and for a given value of Ri_B , the corresponding ζ value can be calculated
 403 using any iterative method.

404 The bulk transfer coefficient for momentum (C_D) and heat (C_H) are defined as:

$$405 C_D = k^2 \left[\ln \left(\frac{z + z_0}{z_0} \right) - \left\{ \psi_m \left(\frac{z + z_0}{L} \right) - \psi_m \left(\frac{z_0}{L} \right) \right\} \right]^{-2} \quad (\text{A8})$$

$$406 C_H = k^2 \left[\ln \left(\frac{z + z_0}{z_0} \right) - \left\{ \psi_m \left(\frac{z + z_0}{L} \right) - \psi_m \left(\frac{z_0}{L} \right) \right\} \right]^{-1} \left[\ln \left(\frac{z + z_h}{z_h} \right) - \left\{ \psi_h \left(\frac{z + z_h}{L} \right) - \psi_h \left(\frac{z_h}{L} \right) \right\} \right]^{-1} \quad (\text{A9})$$

407 Once we get C_D and C_H , then the momentum (τ), and sensible heat (H) fluxes are calculated using the following expressions:

$$408 \tau = \rho C_D U^2 \quad (\text{A10})$$

$$409 H = -\rho c_p C_H U (\theta_a - \theta_g), \quad (\text{A11})$$



410 Appendix B

411 Here, the detailed description of the commonly used similarity functions (φ_m and φ_h) in numerical models under convective
412 conditions is provided.

413 Based on Businger (1966) and A. J. Dyer [1965, unpublished work; see Businger (1988) for details] the expressions
414 for φ_m and φ_h are as follows:

$$415 \varphi_m = (1 - \gamma_m \zeta)^{-\frac{1}{4}} \quad (B1)$$

$$416 \varphi_h = Pr_t (1 - \gamma_h \zeta)^{-\frac{1}{2}} \quad (B2)$$

417 in which $\gamma_m = 15$, $\gamma_h = 9$, and $Pr_t = 0.74$ is the turbulent Prandtl number. Note that in case of Dyer (1974) the values of
418 $\gamma_m = \gamma_h = 16$ and $Pr_t = 1.0$. These functions commonly known as Businger-Dyer similarity (BD) functions and do not
419 satisfy the classical free convection limit (Srivastava et al. 2021).

420 The similarity functions proposed by Carl et al. (1973) under convective conditions are applicable for the range
421 $-10 \leq \zeta \leq 0$. The expressions for φ_m and φ_h suggested by Carl et al. (1973) are:

$$422 \varphi_m = (1 - \beta_m \zeta)^{-\frac{1}{3}} \quad (B3)$$

$$423 \varphi_h = (1 - \beta_h \zeta)^{-\frac{1}{3}} \quad (B4)$$

424 in which $\beta_m = \beta_h = 15$. However, based on various studies reported in the literature β_m and β_h can take different values. For
425 example, Delage and Girard (1992) proposed $\beta_m = \beta_h = 40$, on the other hand, Fairall et al. (1996) suggested that $\beta_m = \beta_h =$
426 12.87.

427 Fairall et al. (1996, 2003) proposed an interpolation function applicable for the entire range of atmospheric instability,
428 which was based on BD functions and functions suggested by Carl et al. (1973). This interpolation function does not have the
429 gradient form (φ_m and φ_h), as they have interpolated the integrated forms of the functions. We wish to highlight that the
430 revised MM5 surface layer scheme of Weather Research and Forecasting Model version 4.2.2 utilized the interpolation
431 functions suggested by Fairall et al. (1996).

432 Kader and Yaglom (1990) proposed a three-sublayer model under convective conditions. According to three sublayer
433 model, in the Dynamic sub-layer (DNS) ($-\frac{1}{40} < \zeta < 0$), $\varphi_m = 1$ and $\varphi_h = Pr_t$. While in the dynamic convective sublayer
434 (DCS) ($-0.4 < \zeta < -\frac{1}{40}$), both φ_m and φ_h varies as a $-1/3$ power law as

$$435 \varphi_m(\zeta) = A_u (-\zeta)^{-\frac{1}{3}} \quad (B5)$$

$$436 \varphi_h(\zeta) = A_T (-\zeta)^{-\frac{1}{3}} \quad (B6)$$

437 in which A_u and A_T are constants.

438 For free convective sublayer ($\zeta < -2$), the theory suggests that φ_m varies as a $1/3$ power law while φ_h varies as a
439 $-1/3$ power law as follows:



440 $\varphi_m(\zeta) = B_u(-\zeta)^{\frac{1}{3}}$ (B7)

441 $\varphi_h(\zeta) = B_T(-\zeta)^{-\frac{1}{3}}$ (B8)

442 in which B_u and B_T are constants.

443 Thus, under unstable conditions, φ_m exhibits a nonmonotonic behaviour with respect to $-\zeta$ as the three sublayer
444 theory suggested that for sufficiently large values of $-\zeta$, φ_m varies as the $+1/3$ power of ζ , in contrast to the case of the free
445 convection limit, where both φ_m and φ_h follow the $-1/3$ power law. In the literature, various expressions for φ_m and φ_h are
446 available based on the Kader and Yaglom (1990) three-sublayer model. However, the present study employs φ_m and φ_h based
447 on the expressions implemented in the surface layer scheme (CLM4.0) of NCAR-CAM5 (Zeng et al., 1998) model. The
448 expressions for φ_m and φ_h utilized in this study are as follows:

449
$$\varphi_m = \begin{cases} (1 - 16\zeta)^{-\frac{1}{4}}, & -1.574 \leq \zeta \leq 0 \\ 0.7k^{\frac{2}{3}}(-\zeta)^{\frac{1}{3}}, & \zeta \leq -1.574 \end{cases}$$
 (B9)

450 and

451
$$\varphi_h = \begin{cases} (1 - 16\zeta)^{-\frac{1}{2}}, & -0.465 \leq \zeta \leq 0 \\ 0.9k^{\frac{4}{3}}(-\zeta)^{-\frac{1}{3}}, & \zeta \leq -0.465 \end{cases}$$
 (B10)

452

453 Srivastava and Sharan (2021) classified these commonly used similarity functions stated above into four different classes based
454 on the exponents appearing in the expressions of φ_m and φ_h . The classification is as follows:

455

456 **Class 1.** This class consists of functions having the exponents of φ_m and φ_h as $-1/4$ and $-1/2$ (as in Eqns. B1 and B2),
457 respectively from near-neutral to strong unstable conditions. φ_m and φ_h proposed by Businger (1971) and Hogstrom (1996)
458 are the examples of class 1 functions.

459

460 **Class 2.** In this class, the similarity functions (φ_m and φ_h) having exponents of φ_m and φ_h as $-1/3$ for the entire range from
461 near-neutral to moderately unstable conditions (as in Eqns. B3 and B4), respectively are included. The functional forms
462 suggested by Carl et al. (1973) are the example of class 2 functions.

463

464 **Class 3.** φ_m and φ_h having exponents as $-1/4$ and $-1/2$, respectively in near neutral conditions while $-1/3$ in strong
465 unstable conditions are included in this class. φ_m and φ_h based on Fairall et al. (1996), Grachev et al. (2000) and Fairall et al.
466 2003 are some examples of class 3 functions.

467

468 **Class 4.** Functional forms of φ_m and φ_h having the exponents as $-1/4$ and $-1/2$, respectively in near neutral conditions
469 however, $1/3$ for φ_m and $-1/3$ for φ_h in strong unstable conditions are classified in this class (as in Eqns. B9 and B10). The



470 three-sublayer model for φ_m and φ_h suggested by Kader and Yaglom (1990) (Zeng et al. 1998) is one of the examples of
471 functions in this class.

472 Appendix C

473 In this section, the details of various physical parameterizations utilized in the real-case simulations using WRFv4.2.2 model
474 and the different statistical indicators used for model evaluation.

475 The real-case simulations with the WRFv4.2.2 model utilised the Purdue Lin microphysics scheme (Lin et al., 1983);
476 YSU (Hong, Noh, and Dudhia, 2006) PBL scheme; Kain-Fritsch (Kain and John, 2004) cumulus scheme; Dudhia (Dudhia,
477 1989) shortwave scheme; RRTM (Mlawer et al., 1997) longwave scheme; Noah-MP land surface model (Niu et al., 2011);
478 and revised MM5 surface layer scheme (Jimenez et al., 2012).

479 In the present study, different statistical indicators have been used for the model evaluation with respect to
480 observations/reanalysis datasets. Statistical parameters such as mean absolute error (MAE), root mean square error (RMSE),
481 mean bias (MB), index of agreement (IOA), and correlation coefficient (CC) are defined as:

482 1. Mean absolute error:

$$483 \quad MAE = \frac{\sum_{i=1}^n |p_i - o_i|}{n}$$

484 2. Root mean square error:

$$485 \quad RMSE = \sqrt{\frac{\sum_{i=1}^n (p_i - o_i)^2}{n}}$$

486 3. Mean bias

$$487 \quad MB = (\bar{p} - \bar{o})$$

488 4. Index of agreement

$$489 \quad IOA = 1 - \frac{\sum_{i=1}^n (o_i - p_i)^2}{\sum_{i=1}^n (|p_i - \bar{o}| + |o_i - \bar{o}|)^2}$$

490 5. Correlation coefficient

$$491 \quad CC = \frac{\sum_{i=1}^n (p_i - \bar{p})(o_i - \bar{o})}{\sqrt{\sum_{i=1}^n (p_i - \bar{p})^2} \sqrt{\sum_{i=1}^n (o_i - \bar{o})^2}}$$

492 in which p_i and o_i represent the predicted and observed time series, respectively, while \bar{p} and \bar{o} are the predicted
493 and observed mean for a considered variable, respectively.

494 6. Taylor diagram: It exhibits how well patterns match each other in terms of their correlation, ratio of their variances,
495 and root mean square differences (Taylor, 2001).

496 7. Q-Q plot: It is a graphical technique used to compare the overall distribution of predicted and observed values for a
497 variable (Venkatram, 1999)



498 The error or deviation between observed and simulated values is measured by MAE, RMSE, and MB. On the other
499 hand, IOA is used to assess the trend relationship, or how closely the magnitudes and signs of the observed values are related
500 to the projected values (Schlunzen and Sokhi 2008). In order to evaluate the spatial patterns with ERA5-Land reanalysis
501 dataset, statistical metrics such as mean bias (%), RMSE, and pattern correlation (PCC) have been used.

502 **Code and data availability:** Weather Research and Forecasting Model version 4.2.2 (WRFv4.2.2) is an open source model
503 and can be downloaded from https://www2.mmm.ucar.edu/wrf/users/download/get_source.html. The model output at the
504 location of the flux tower at Ranchi (23.412N, 85.440E), India is openly available at <https://doi.org/10.5281/zenodo.10435513>.
505 The raw observational data derived from the flux tower at Ranchi (23.412N, 85.440E; India) utilized in the present study can
506 be obtained from the Indian National Centre for Ocean Information Service upon request
507 (<http://www.incois.gov.in/portal/datainfo/ctczdata.jsp>). Hourly ERA5-Land reanalysis data utilized in this study can be found
508 in its official website <https://cds.climate.copernicus.eu/cdsapp#!/dataset/reanalysis-era5-land?tab=form>.

509 **Author contribution:** All authors contributed to the design of the study, analysis, and writing of the manuscript. PN carried
510 out the computations as well as the analysis of the model output.

511 **Competing interests:** The authors have declared that they have no conflict of interest.

512 **Acknowledgements:**

513 We would like to thank Dr. Manoj Kumar for providing observational data at Ranchi. The authors acknowledge the use of
514 NCAR-NCL and ERA5-Land reanalysis dataset for this study. The use of supercomputing facility (HPC) provided by IIT
515 Delhi is gratefully acknowledged. This work is partially supported by INSA, DST, DST-INSPIRE, and YES Foundation.

516 **References:**

517 Bruin, H. A. R. de.: A Note on Businger's Derivation of Nondimensional Wind and Temperature Profiles under Unstable
518 Conditions, *J. Appl. Meteor. Climatol.*, 38, 626–28, [https://doi.org/10.1175/1520-0450\(1999\)038<0626:ANOBSD>2.0.CO;2](https://doi.org/10.1175/1520-0450(1999)038<0626:ANOBSD>2.0.CO;2),
519 1999.
520 Brutsaert, W.: Stability Correction Functions for the Mean Wind Speed and Temperature in the Unstable Surface Layer,
521 *Geophys. Res. Lett.*, 19, 469–72. <https://doi.org/10.1029/92GL00084>, 1992.



- 522 Businger, J. A., Wyngaard, J. C., Izumi, Y., & Bradley, E. F. 1971. “Flux-Profile Relationships in the Atmospheric Surface
523 Layer in the Atmospheric Surface Layer”. *J. Atmos. Sci.*, 28(2), 181-189. [https://doi.org/10.1175/1520-0469\(1971\)028<0181:FPRITA>2.0.CO;2](https://doi.org/10.1175/1520-0469(1971)028<0181:FPRITA>2.0.CO;2), 1971.
- 525 Carl, D. M., Tarbell, T. C., and Panofsky, H. A.: Profiles of Wind and Temperature from Towers over Homogeneous Terrain,
526 *J. Atmos. Sci.*, 30, 788-794, [http://dx.doi.org/10.1175/1520-0469\(1973\)030<0788:POWATF>2.0.CO;2](http://dx.doi.org/10.1175/1520-0469(1973)030<0788:POWATF>2.0.CO;2), 1973.
- 527 Cheng, Y., and Brutsaert, W.: Flux-Profile Relationships for Wind Speed and Temperature in the Stable Atmospheric
528 Boundary Layer, *Boundary-Layer Meteorol.*, 114, 519–38. <https://doi.org/10.1007/s10546-004-1425-4>, 2005.
- 529 Dwivedi, A. K., Chandra, S., Kumar, M., Kumar, S., and Kumar, N. V. P. K.: Spectral Analysis of Wind and Temperature
530 Components during Lightning in Pre-Monsoon Season over Ranchi, *Meteorol. Atmos. Phys.*, 127, 95–105,
531 <https://doi.org/10.1007/s00703-014-0346-0>, 2015.
- 532 Dyer, A. J.: A Review of Flux-Profile Relationships, *Boundary-Layer Meteorol.*, 7, 363–372.
533 <https://doi.org/10.1007/BF00240838>, 1974.
- 534 Fairall, C. W., Bradley, E. F., Hare, J. E., Grachev, A. A., and Edson, J. B.: Bulk Parameterization of Air–Sea Fluxes: Updates
535 and Verification for the COARE Algorithm, *J. Climate*, 16, 571–591, [https://doi.org/10.1175/1520-0442\(2003\)016<0571:BPOASF>2.0.CO;2](https://doi.org/10.1175/1520-0442(2003)016<0571:BPOASF>2.0.CO;2), 2003.
- 537 Fairall, C. W., Bradley, E. F., Rogers, D. P., Edson, J. B., and Young, G. S.: Bulk Parameterization of Air-Sea Fluxes for
538 Tropical Ocean global Atmosphere Coupled-Ocean Atmosphere Response Experiment, *J. Geophys. Res.*, 101, 3747–3764,
539 doi:[10.1029/95JC03205](https://doi.org/10.1029/95JC03205), 1996.
- 540 Friedl, M. A., McIver, D. K., Hodges, J. C. F., Zhang, X. Y., Muchoney, D., Strahler, A. H., Woodcock, C. E., Gopal, S.,
541 Schneider, A., Cooper, A., Baccini, A., Gao, F., and Schaaf, C.: Global Land Cover Mapping from MODIS: Algorithms and
542 Early Results, *Remote Sens. Environ.* 83, 287–302, [https://doi.org/10.1016/S0034-4257\(02\)00078-0](https://doi.org/10.1016/S0034-4257(02)00078-0), 2002.
- 543 Giorgi, F., Coppola, E., Solmon, F., Mariotti, L., Sylla, M. B., Bi, X., Elguindi, N., et al.: RegCM4: Model Description and
544 Preliminary Tests over Multiple CORDEX Domains, *Clim. Res.*, 52, 7–29, <http://doi.org/10.3354/cr01018>, 2012.
- 545 Grachev, A. A., Fairall, C. W., and Bradley, E. F.: Convective Profile Constants Revisited, *Boundary-Layer Meteorol.*, 94,
546 495–515, <https://doi.org/10.1023/A:1002452529672>, 2000.
- 547 Grachev, A. A., Andreas, E. L., Fairall, C. W., Guest, P. S., and Persson, P. O. G.: SHEBA Flux-Profile Relationships in the
548 Stable Atmospheric Boundary Layer, *Boundary-Layer Meteorol.*, 124, 315–33, <https://doi.org/10.1007/s10546-007-9177-6>,
549 2007.
- 550 Grell, G. A., Dudhia, J., & Stauffer, D.: A description of the fifth-generation Penn State/NCAR Mesoscale Model (MM5) (No.
551 NCAR/TN-398+STR), University Corporation for Atmospheric Research. <http://doi:10.5065/D60Z716B>, 1994.
- 552 Hicks, B. B.: Wind Profile Relationships from the ‘Wangara’ Experiment, *Q. J. R. Meteorol. Soc.*, 102, 535–51,
553 <https://doi.org/10.1002/qj.49710243304>, 1976.
- 554 Hogstrom, U.: Review of Some Basic Characteristics of the Atmospheric Surface Layer, *Boundary-Layer Meteorol.*, 78, 215–
555 246, <https://doi.org/10.1007/BF00120937>, 1996.



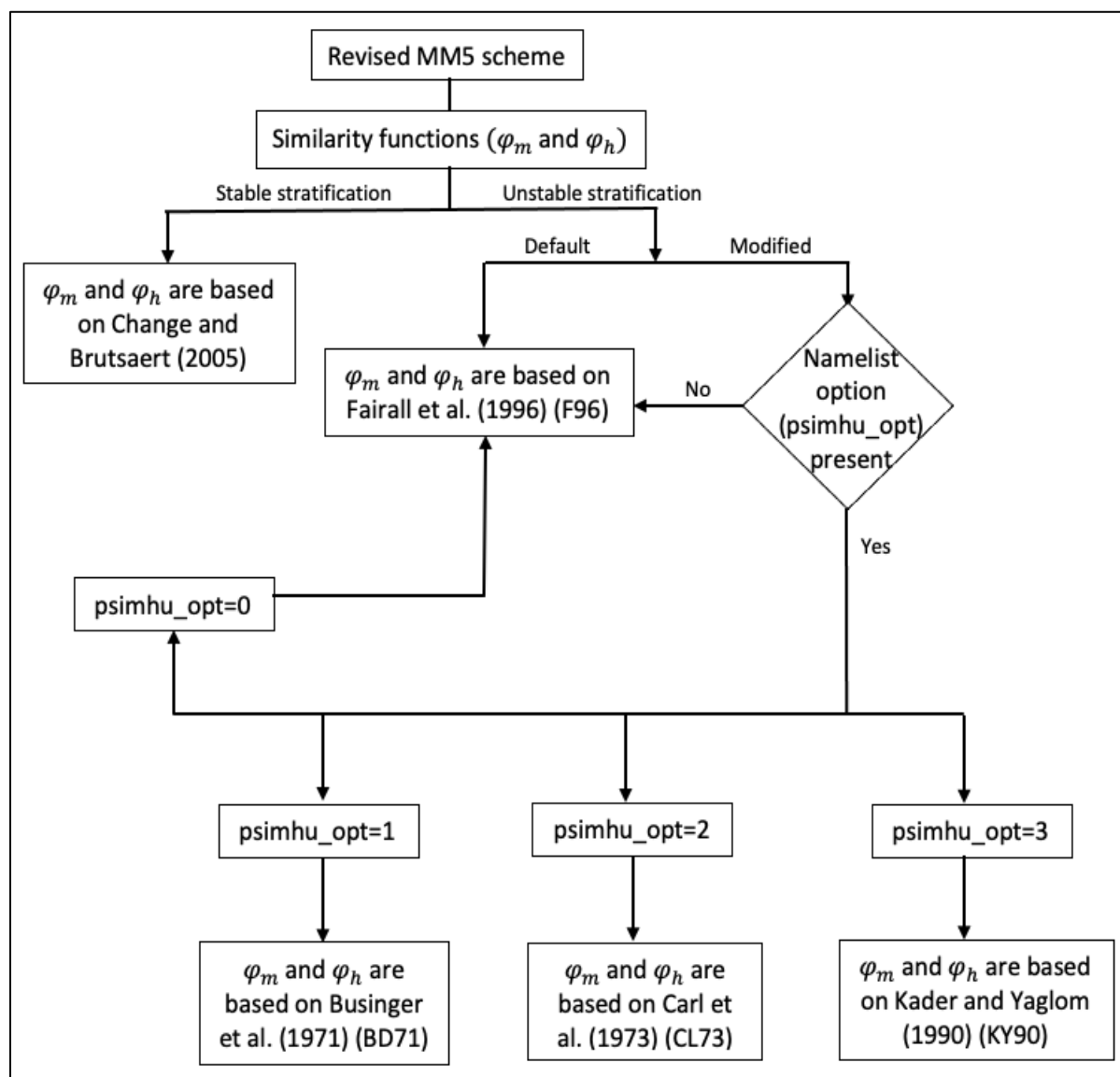
- 556 Holtslag, A. A. M., and De Bruin, H. A. R.: Applied Modeling of the Night-time Surface Energy Balance over Land, *J. Appl.*
557 *Meteor. Climatol.*, 27, 689-704. [https://doi.org/10.1175/1520-0450\(1988\)027<0689:AMOTNS>2.0.CO;2](https://doi.org/10.1175/1520-0450(1988)027<0689:AMOTNS>2.0.CO;2), 1988.
- 558 Jiménez, P. A., González-Rouco, J. F., García-Bustamante, E., Navarro, J., Montávez, J. P., de Arellano, J. V., Dudhia, J., &
559 Muñoz-Roldan, A.: Surface Wind Regionalization over Complex Terrain: Evaluation and Analysis of a High-Resolution WRF
560 Simulation, *J. Appl. Meteor. Climatol.*, 49, 268-287, <https://doi.org/10.1175/2009JAMC2175.1>, 2010.
- 561 Jiménez, P. A., Dudhia, J., González-Rouco, J. F., Navarro, J., Montávez, J. P., & García-Bustamante, E.: A Revised Scheme
562 for the WRF Surface Layer Formulation, *Mon. Wea. Rev.*, 140, 898-918. <https://doi.org/10.1175/MWR-D-11-00056.1>, 2012.
- 563 Kader, B. A., and Yaglom, A. M.: Mean Fields and Fluctuation Moments in Unstably Stratified Turbulent Boundary Layers,
564 *Journal of Fluid Mechanics*, 212, 637–662, <https://doi.org/10.1017/S0022112090002129>, 1990.
- 565 Monin, A. S., and Obukhov, A. M.: Basic Laws of Turbulent Mixing in the Surface Layer of the Atmosphere, *Tr. Akad. Nauk*
566 *SSSR Geophys. Inst* 24(151), 163–187, 1954.
- 567 Namdev, P., Sharan, M. & Mishra, S.K.: Impact of the similarity functions of surface layer parametrization in a climate model
568 over the Indian region, *Q. J. R. Meteorol. Soc.*, 149, 152–170, <https://doi.org/10.1002/qj.4400>, 2023.
- 569 Panofsky, H. and Dutton, J.: *Atmospheric Turbulence*, John Wiley & Sons, New York, 397 p, 1984.
- 570 Rao, K. G., Narasimha, R., and Prabhu, A.: Estimation of Drag Coefficient at Low Wind Speeds over the Monsoon Trough
571 Land Region during MONTBLEX-90, *Geophys. Res. Lett.*, 23, 2617–2620, <https://doi.org/10.1029/96GL02368>, 1996.
- 572 Rao, K. G., and Narasimha, R.: Heat-Flux Scaling for Weakly Forced Turbulent Convection in the Atmosphere, *Journal of*
573 *Fluid Mechanics*, 547, 115–135, <https://doi.org/10.1017/S0022112005007251>, 2006.
- 574 Sharan, M., and Srivastava, P.: Characteristics of the Heat Flux in the Unstable Atmospheric Surface Layer, *J. Atmos. Sci.*,
575 73, 4519–4529, <https://doi.org/10.1175/JAS-D-15-0291.1>, 2016.
- 576 Srivastava, P., and Sharan, M.: Characteristics of the Drag Coefficient over a Tropical Environment in Convective Conditions,
577 *J. Atmos. Sci.*, 72, 4903–4913, <https://doi.org/10.1175/JAS-D-14-0383.1>, 2015.
- 578 Srivastava, P., and Sharan, M.: Analysis of Dual Nature of Heat Flux Predicted by Monin-Obukhov Similarity Theory: An
579 Impact of Empirical Forms of Stability Correction Functions, *J. Geophys. Res. Atmos.*, 124, 3627–3646,
580 <https://doi.org/10.1029/2018JD029740>, 2019.
- 581 Srivastava, P., and Sharan, M.: Uncertainty in the Parameterization of Surface Fluxes under Unstable Conditions, *J. Atmos.*
582 *Sci.*, 78, 2237–2247, <https://doi.org/10.1175/JAS-D-20-0350.1>, 2021.
- 583 Srivastava, P., Sharan, M., and Kumar, M.: A Note on Surface Layer Parameterizations in the Weather Research and Forecast
584 Model, *Dynam. Atmos. Ocean*, 96, 101259, <https://doi.org/10.1016/j.dynatmoce.2021.101259>, 2021.
- 585 Srivastava, P., Sharan, M., Kumar, M., and Dhuria, A. K.: On Stability Correction Functions over the Indian Region under
586 Stable Conditions, *Meteorol. Appl.*, 27:e1880, <https://doi.org/10.1002/met.1880>, 2020.
- 587 Stull, R. B.: *An Introduction to Boundary Layer Meteorology*, Kluwer Academic Publishers, Dordrecht, The Netherlands, 13,
588 670 pp, <https://doi.org/10.1007/978-94-009-3027-8>, 1988.



- 589 Venkatram, A.: Applying a framework for evaluating the performance of air quality models, in: Proceedings of the sixth
590 International Conference on Harmonisation within Atmospheric Dispersion modeling for Regulatory Applications, Rouen,
591 France, 11 – 14 October, 1999, 11 – 14, 1999.
- 592 Webb, E. K.: Profile Relationships: The Log-linear Range, and Extension to Strong Stability, Q. J. R. Meteorol. Soc., 96, 67–
593 90, <https://doi.org/10.1002/qj.49709640708>, 1970.
- 594 Wilson, D. K.: An Alternative Function for the Wind and Temperature Gradients in Unstable Surface Layers, Boundary-Layer
595 Meteorol., 99, 151–158, <https://doi.org/10.1023/A:1018718707419>, 2001.
- 596 Zeng, X., Zhao, M., and Dickinson, R. E.: Intercomparison of Bulk Aerodynamic Algorithms for the Computation of Sea
597 Surface Fluxes Using TOGA COARE and TAO Data, J. Climate, 11, 2628–2644, [https://doi.org/10.1175/1520-0442\(1998\)011<2628:IOBAAF>2.0.CO;2](https://doi.org/10.1175/1520-0442(1998)011<2628:IOBAAF>2.0.CO;2), 1998.
- 599



600

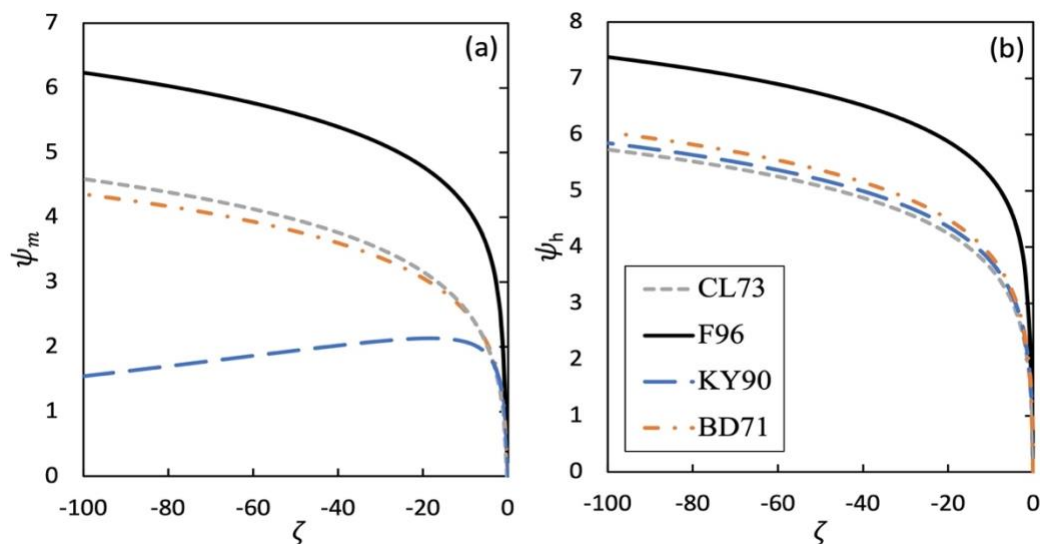


601 Figure 1: Flowchart to provide a brief description of different options for similarity functions in the modified surface layer scheme
602 that can be controlled by namelist variable psimhu_opt.

603



604



605 **Figure 2: Integrated similarity functions $\psi_{m,h}(\zeta)$ for momentum and heat for default and incorporated functions for unstable**
606 **atmospheric surface layer.**

607

608

609

610

611

612

613

614

615

616

617

618

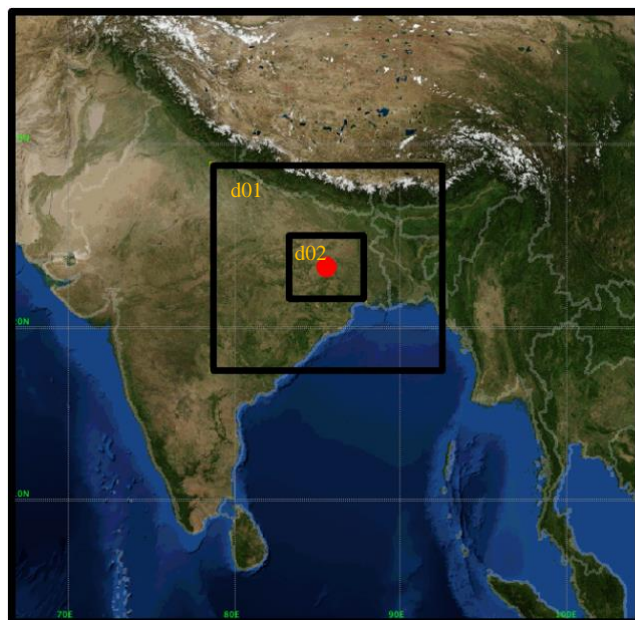
619

620

621

622

623

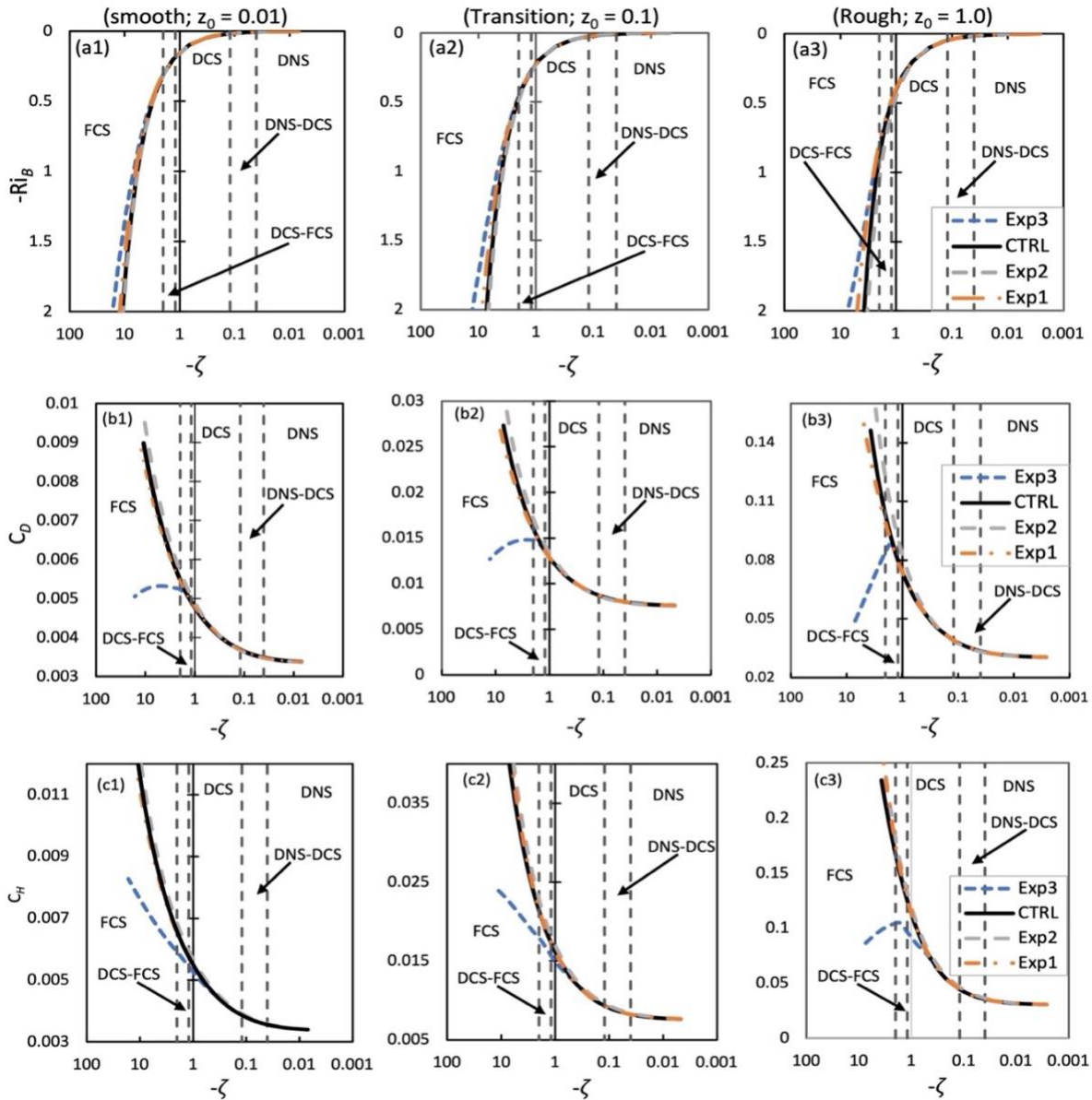


624 **Figure 3: Spatial distribution of domain used for the simulations using WRF model. The spatial resolution for domains d01 and d02**
625 **is 6×6 km and 2×2 km, respectively. The domain d02 covers 446×392 km² area around the centre point.**



626

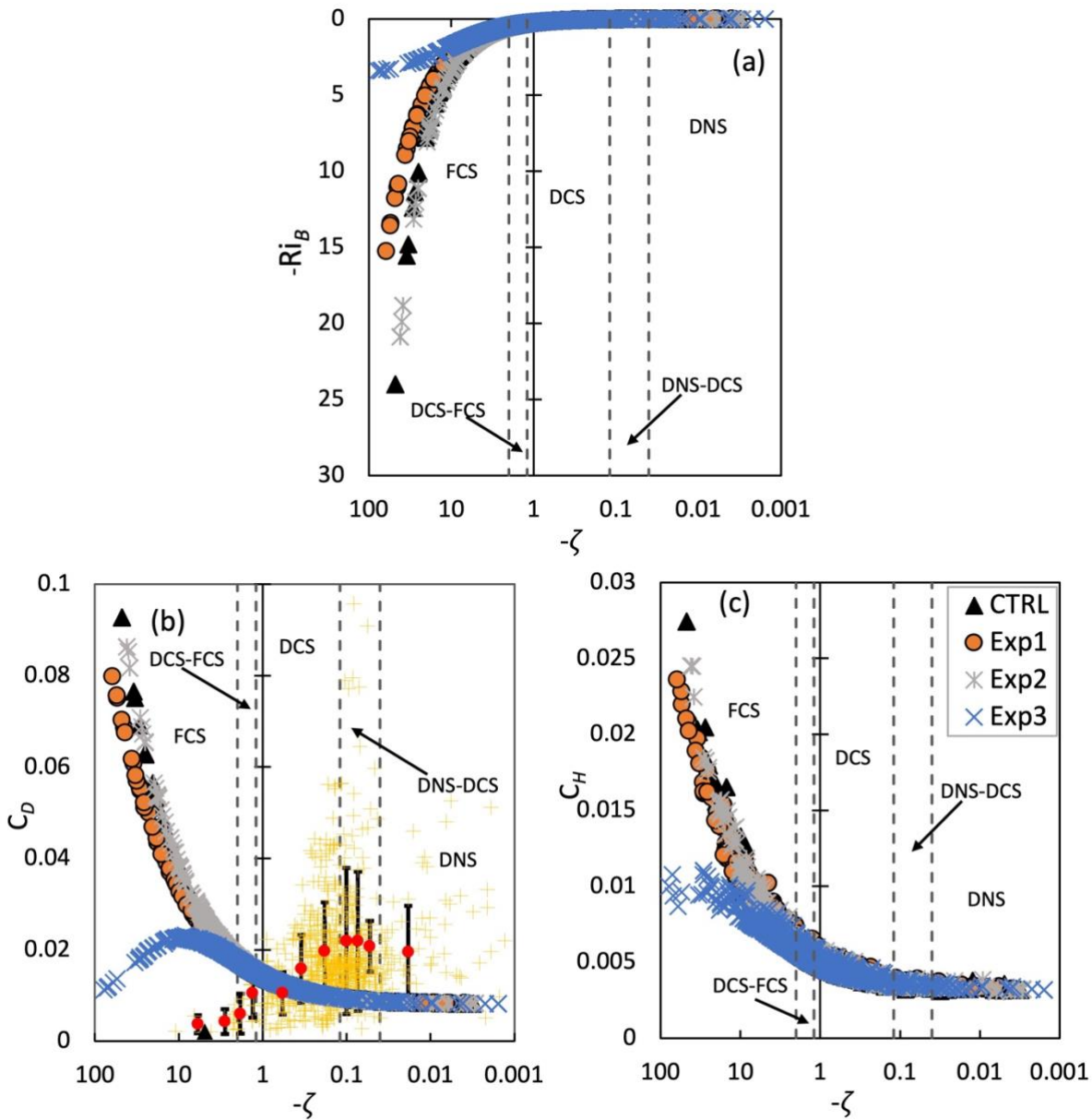
627



628 **Figure 4: Variation of ζ with Ri_B (upper panel), C_D (middle panel) and C_H (lower panel) with ζ calculated from bulk flux algorithm**
 629 **(offline simulation) for different experiments corresponding to different functional forms of ψ_m and ψ_h together with the CTRL**
 630 **simulation for smooth ($z_0 = 0.01$ m; 1st column), transition ($z_0 = 0.1$ m; second column), and rough ($z_0 =$**
 631 **1.0 m; third column) surfaces. The dotted lines separate different sublayer within the convective regime.**

632

633



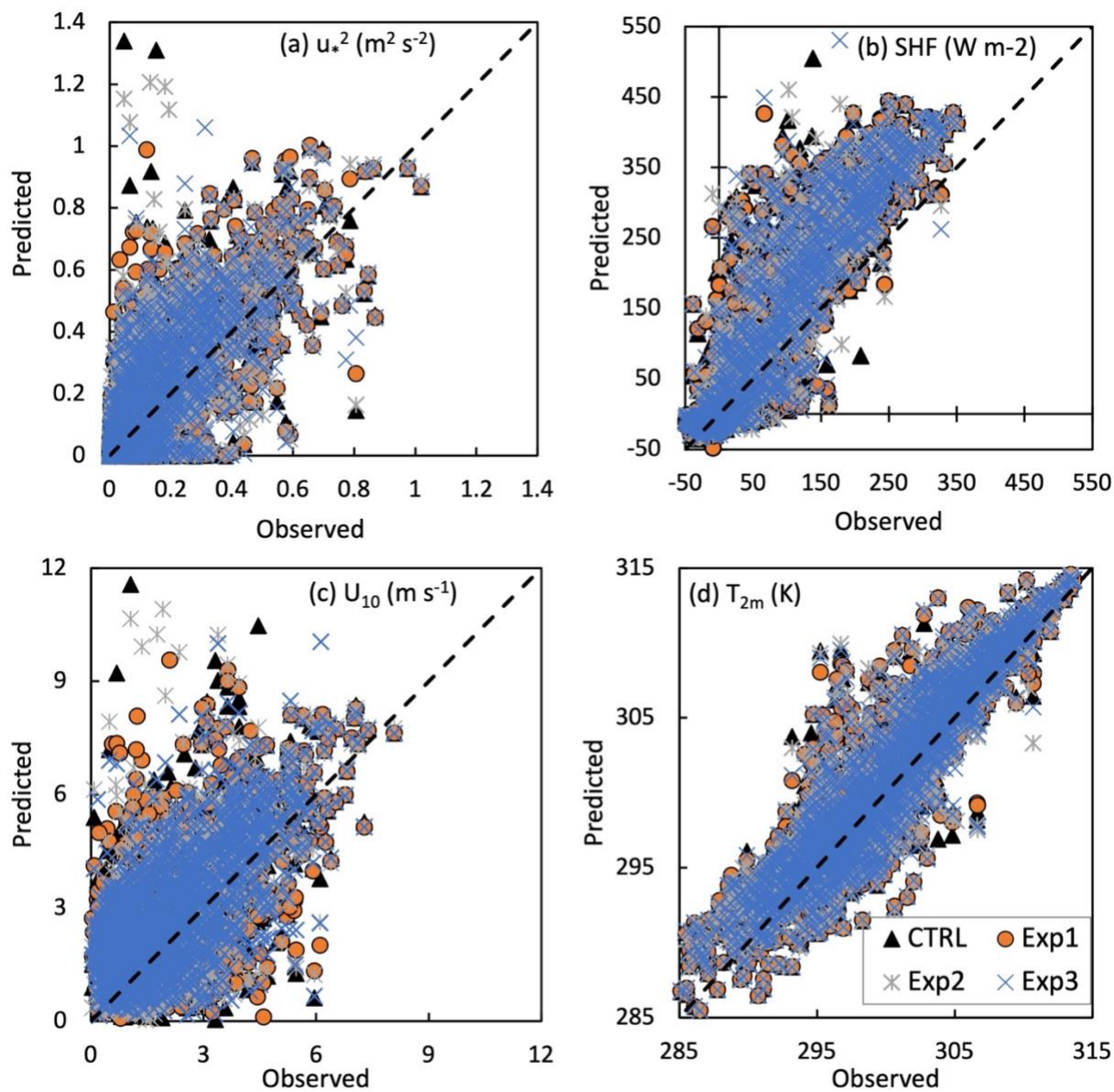
634

635 **Figure 5: Variation of model simulated (a) ζ with Ri_B , (b) C_D and (c) C_H with ζ from different experiments using different ψ_m and**
 636 **ψ_h corresponding to F96 (CTRL), BD71 (Exp1), CL73 (Exp2), and KY90 (Exp3) under convective conditions. The yellow markers**
 637 **(+) in (b) denote the observed C_D with ζ at the location of flux tower. The dotted lines separate different sublayer within the**
 638 **convective regime. The mean values of observed C_D in each sublayer are shown with red dots along with standard deviations in the**
 639 **form of error bars. Depending upon the data availability, two or three bins of equal width are chosen in each sublayer.**

640



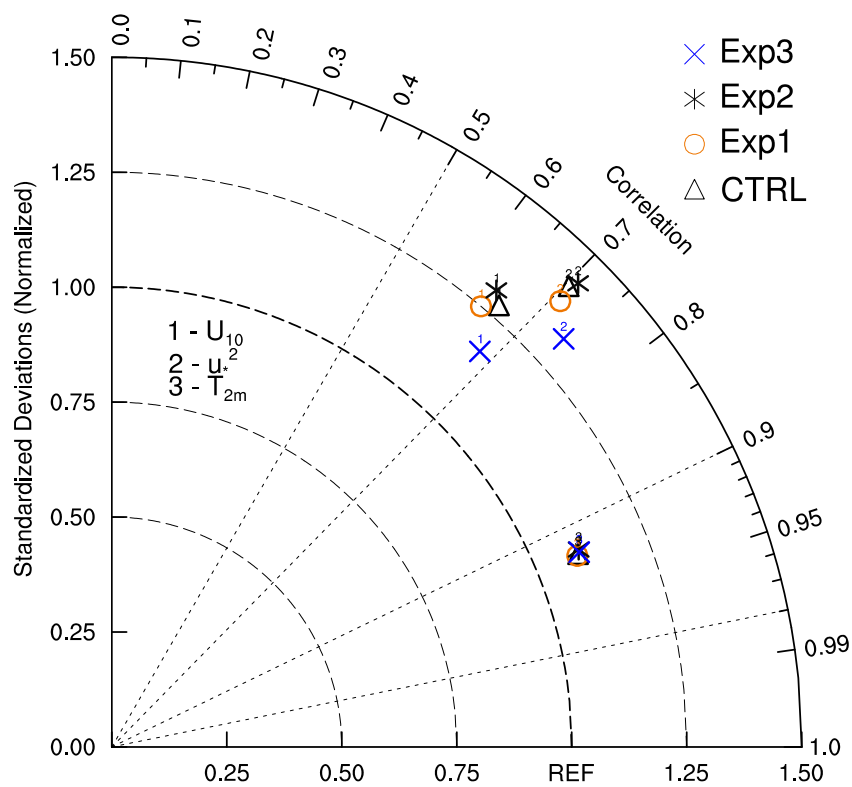
641



642 **Figure 6:** Scatter plot of model simulated (a) u_*^2 ($\text{m}^2 \text{s}^{-2}$) (representative of momentum flux), (b) SHF (W m^{-2}) (sensible heat flux), (c)
643 U_{10} (m s^{-1}) (wind speed at 10 m height), and (d) T_{2m} (K) (temperature at 2 m height) vs observed values at the location of flux tower
644 at Ranchi (23.412oN, 85.440oE), India (centre point of the domain) during pre-monsoon season (MAM).

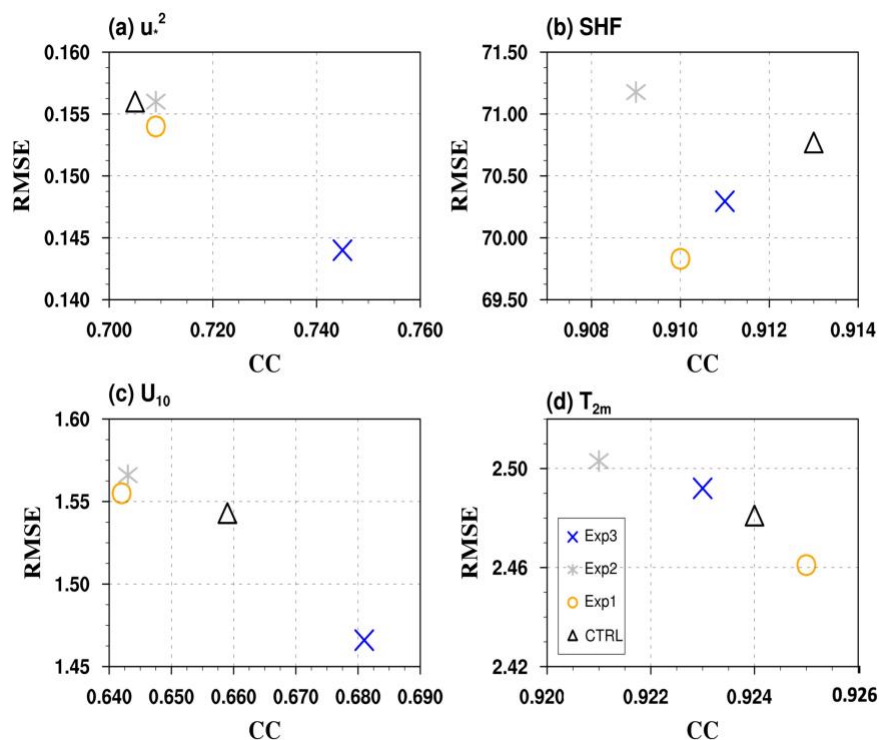
645

646



647

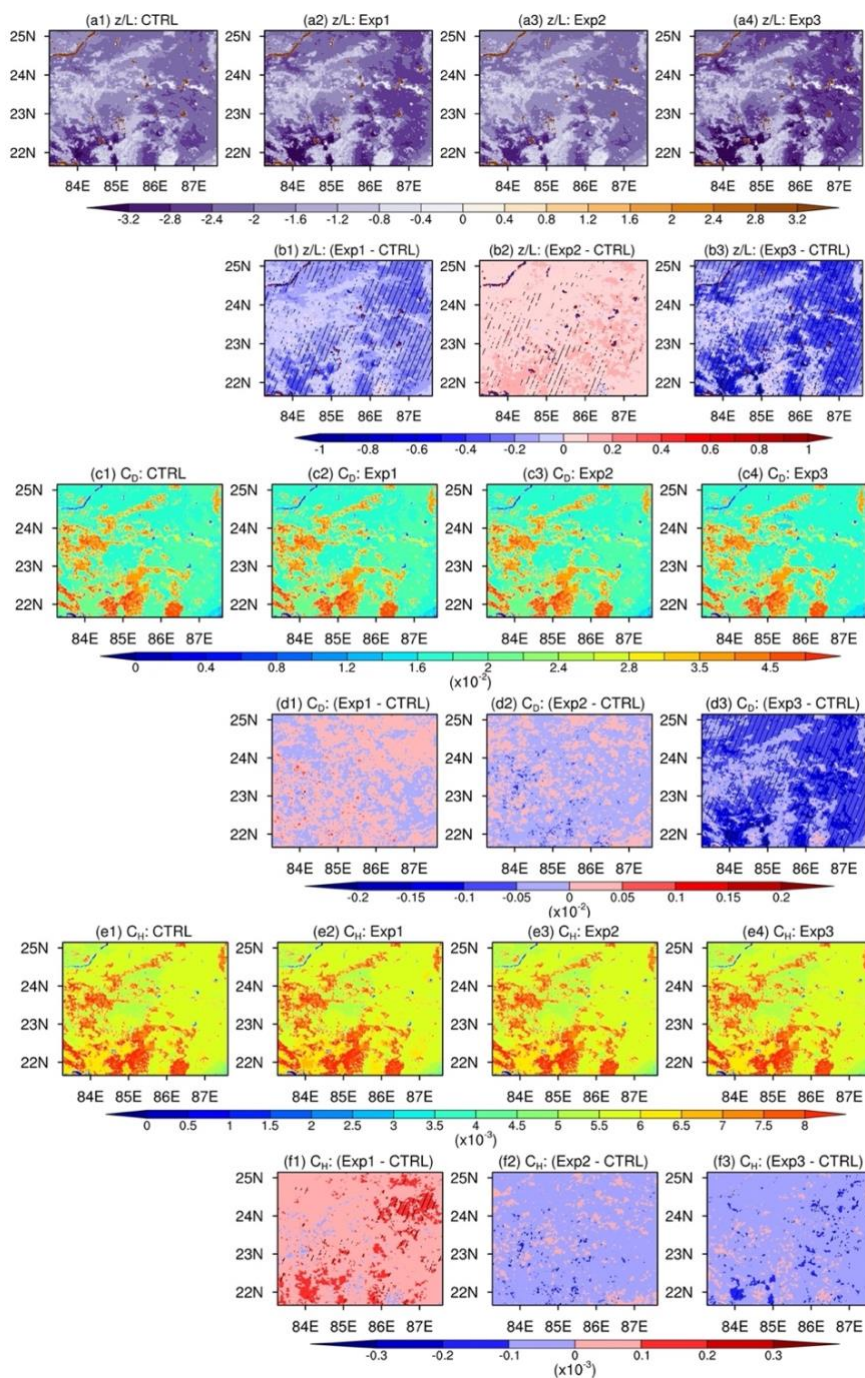
648 **Figure 7: Taylor diagram showing the correlation coefficient, normalized standard deviations for U_{10} , u_{*2}^2 , and T_{2m} from different**
649 **experiments together with CTRL simulation with respect to observations derived from flux tower installed at Ranchi (23.412°N,**
650 **85.440°E), India.**



651

652 **Figure 8: Scatter plot between correlation coefficient (CC) and root mean square error (RMSE) for (a) u_*^2 , (b) SHF, (c) U_{10} , and (d)**
653 **T_{2m} simulated by various experiments (Exp1-3) together with CTRL simulation for pre-monsoon season (MAM; 2009) at the location**
654 **of the flux tower (23.412°N, 85.440°E).**

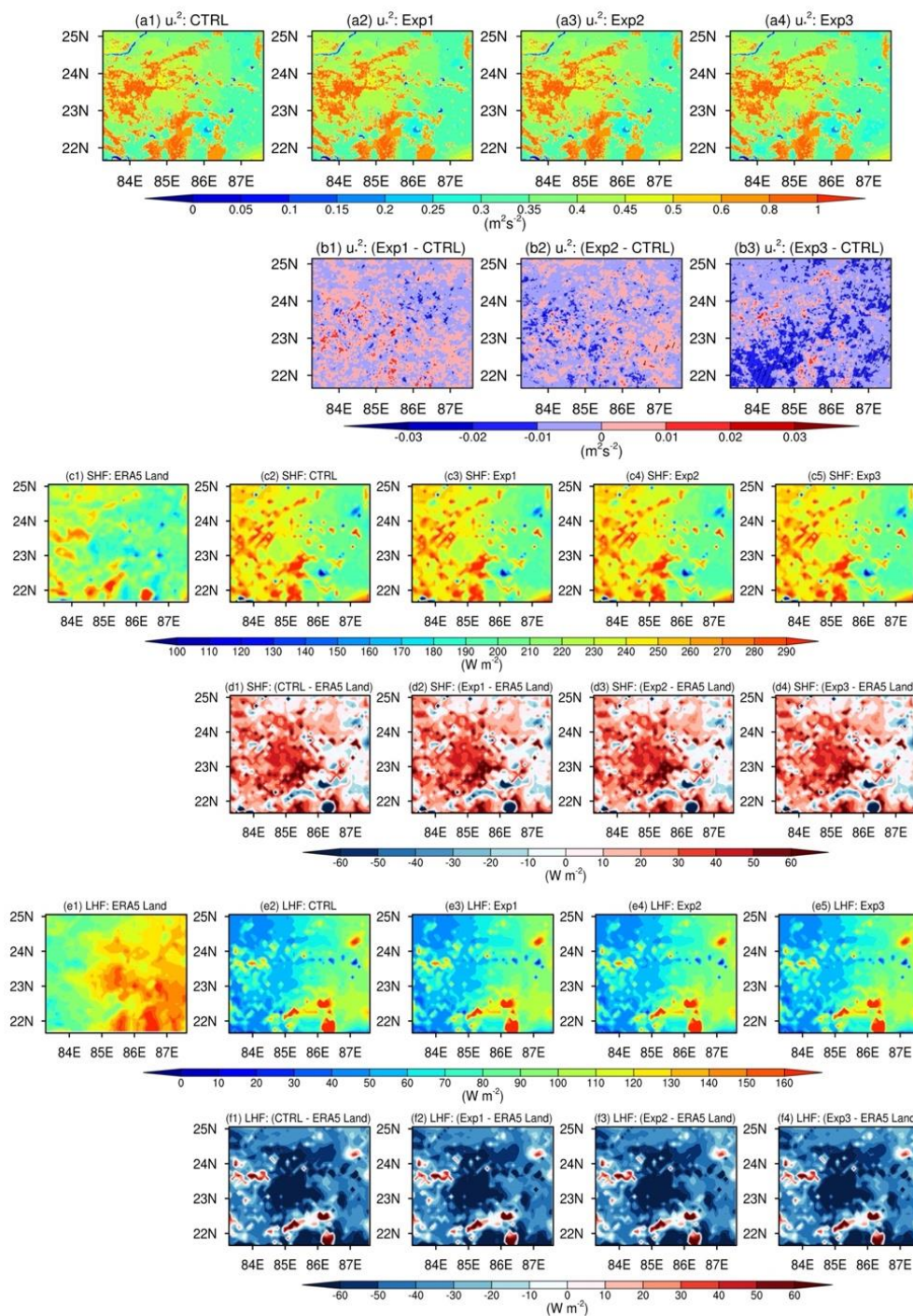
655



656

657 **Figure 9: Mean spatial distribution of model simulated ζ (1st row), C_D (3rd row) and C_H (5th row) from different experiments and**
 658 **their differences with respect to CTRL simulation averaged during daytime for whole simulation period. Hatched regions show**
 659 **significant differences at 95% confidence level in experiments with respect to CTRL simulation.**

660

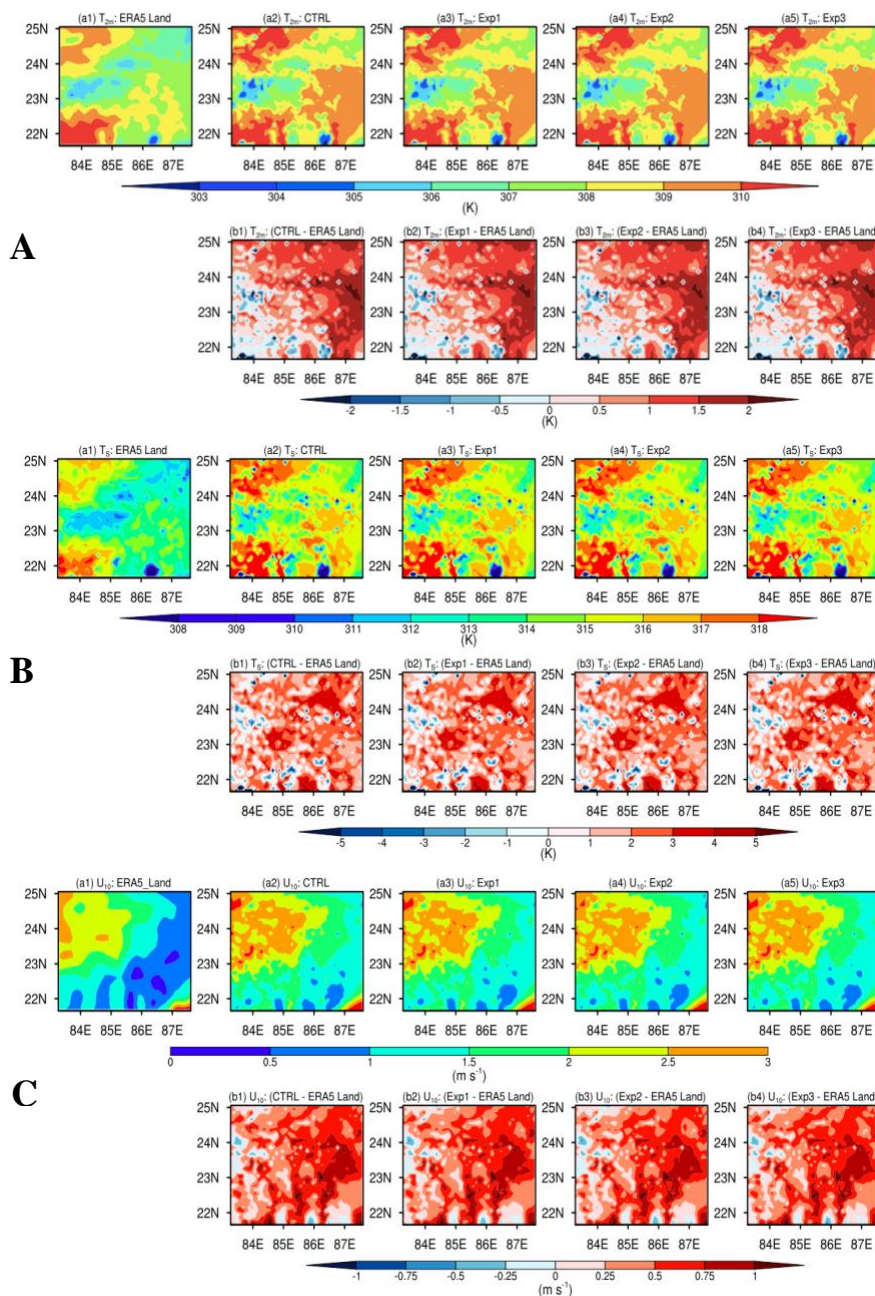


661

662 **Figure 10: Mean spatial distribution of simulated u_*^2 (1st row) from different experiments and their differences (2nd row) with respect to CTRL simulation. SHF and LHF from ERA5-Land reanalysis and simulated using various experiments and their differences**
 663 **to CTRL simulation. SHF and LHF from ERA5-Land reanalysis and simulated using various experiments and their differences**
 664 **with respect to ERA5-Land data averaged during daytime for the whole simulation period are shown. Hatched regions show**
 665 **significant differences at 95% confidence level in experiments with respect to CTRL simulation.**

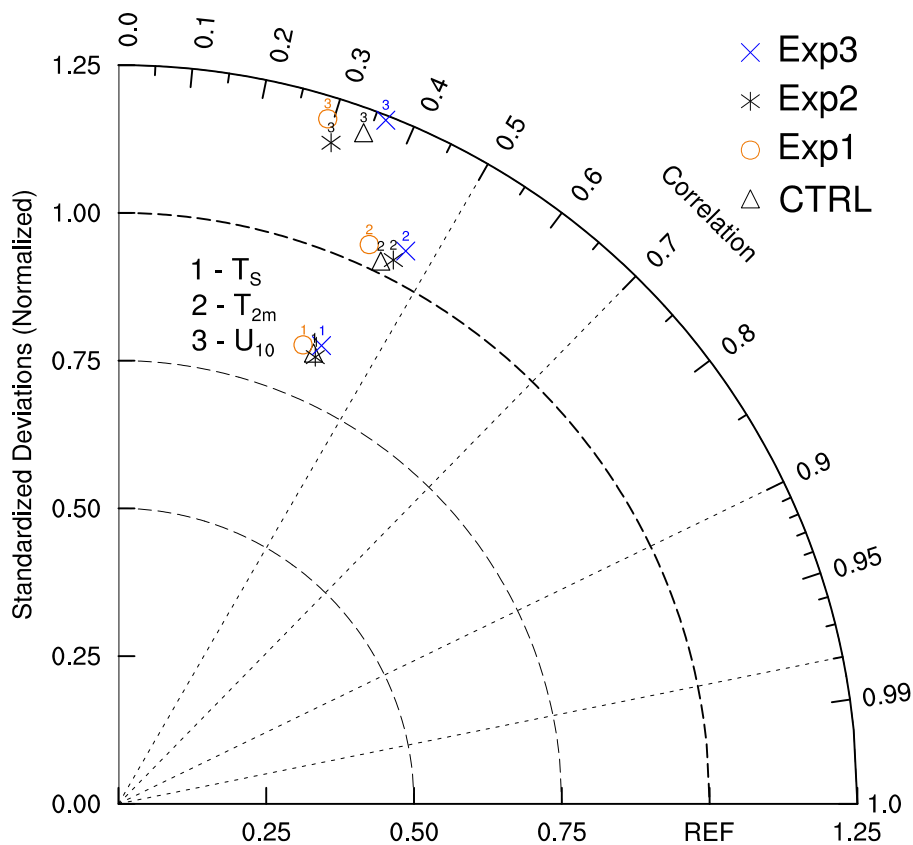


666



667 **Figure 11:** In upper panel (A), mean spatial distribution of T_{2m} from ERA5-Land reanalysis (a1) and simulated using different
 668 experiments (a2-a5) and their differences with respect to ERA5-Land reanalysis (b1-b4) averaged during daytime for the whole
 669 simulation period. Middle (Lower) panel is same as the upper panel but for T_s (U_{10}).

670



671

672 **Figure 12: Taylor diagram showing the correlation coefficient, normalized standard deviations for T_s (K), T_{2m} (K), and U_{10} ($m s^{-1}$)**
673 **from different experiments together with CTRL simulation with respect to ERA5-Land reanalysis dataset averaged during strong**
674 **convective conditions (hours during daytime in which ζ is smaller than -10) for whole simulation period.**

675

676

677



Experiments	Description
CTRL	Simulation using default surface layer scheme with F96 functions
Exp1	Simulation using surface layer scheme with BD71 functions
Exp2	Simulation using surface layer scheme with CL73 functions
Exp3	Simulation using surface layer scheme with incorporated KY90 functions

678 **Table 1. Description of various simulations conducted in this study.**

679
680
681
682
683
684
685
686
687
688
689
690
691
692
693
694
695
696
697
698
699



700

MAM		u_*^2 ($\text{m}^2 \text{s}^{-2}$)	SHF (W m^{-2})	U_{10} (m s^{-1})	T_{2m} (K)
CTRL	MAE	0.088	43.456	1.198	1.815
	RMSE	0.156	70.770	1.543	2.481
	MB	0.034	34.876	0.825	0.926
	IOA	0.818	0.896	0.729	0.954
	CC	0.705	0.913	0.659	0.924
Exp1	MAE	0.086	42.719	1.207	1.807
	RMSE	0.154	69.830	1.555	2.461
	MB	0.031	33.064	0.812	0.896
	IOA	0.823	0.898	0.720	0.955
	CC	0.709	0.910	0.642	0.925
Exp2	MAE	0.088	43.547	1.200	1.835
	RMSE	0.156	71.177	1.566	2.503
	MB	0.032	34.486	0.812	0.873
	IOA	0.822	0.894	0.721	0.954
	CC	0.709	0.909	0.643	0.921
Exp3	MAE	0.082	42.960	1.164	1.833
	RMSE	0.144	70.295	1.466	2.492
	MB	0.026	33.472	0.782	0.908
	IOA	0.843	0.897	0.751	0.954
	CC	0.742	0.911	0.681	0.923

701

702 **Table 2: Comparison statistics for u_*^2 ($\text{m}^2 \text{s}^{-2}$), SHF (W m^{-2}), U_{10} (m s^{-1}), and T_{2m} (K) simulated using different experiments together**
 703 **with CTRL simulation with respect to observations derived from flux tower at Ranchi (India) for MAM season. The mean absolute**
 704 **error (MAE), root mean square error (RMSE), mean bias (MB), index of agreement (IOA), and correlation coefficient (CC) are**
 705 **shown.**

706

707

708

709

710

711

712

713



714

MAM	T _s (K)			T _{2m} (K)			U ₁₀ (m s ⁻¹)		
	Bias (%)	RMSE	PCC	Bias (%)	RMSE	PCC	Bias (%)	RMSE	PCC
CTRL	1.259	4.013	0.397	0.635	2.133	0.435	-4.962	0.438	0.343
Exp1	1.261	4.030	0.373	0.638	2.157	0.409	-4.430	0.454	0.292
Exp2	1.252	3.989	0.403	0.626	2.103	0.451	-5.386	0.442	0.306
Exp3	1.243	3.972	0.405	0.623	2.102	0.461	-0.284	0.474	0.364

715

716 **Table 3: Comparison statistics for T_{2m} (K), T_s (K), and U₁₀ (m s⁻¹) simulated using different experiments together with CTRL**
 717 **simulation with respect to ERA5-Land reanalysis data averaged during strong unstable stratification (hours during daytime in**
 718 **which ζ is smaller than -10) for whole simulation period. The percent mean bias (Bias %), pattern correlation coefficient (PCC),**
 719 **and root mean square error (RMSE) are shown.**

720

721